J. Fluid Mech. (2010), *vol.* 651, *pp.* 165–209.
doi:10.1017/S0022112009993958

Direct simulation of turbulent swept flow over a wire in a channel

R. RANJAN[1]†, C. PANTANO[1] AND P. FISCHER[2]

[1]Department of Mechanical Science and Engineering, University of Illinois at Urbana-Champaign, 1206 West Green Street, Urbana, IL 61801, USA

[2]Mathematics and Computer Science Division, Argonne National Laboratory, Argonne, IL 60439, USA

(Received 1 June 2009; revised 8 December 2009; accepted 9 December 2009; first published online 29 March 2010)

Turbulent swept flow over a cylindrical wire placed on a wall of a channel is investigated using direct numerical simulations. This geometry is a model of the flow through the wire-wrapped fuel pins, the heat exchanger, typical of many nuclear reactor designs. Mean flow along and across the wire axis is imposed, leading to the formation of separated flow regions. The Reynolds number based on the bulk velocity along the wire axis direction and the channel half height is 5400 and four cases are simulated with different flowrates across the wire. This configuration is topologically similar to backward-facing steps or slots with swept flow, except that the dominant flow is along the obstacle axis in the present study and the crossflow is smaller than the axial flow, i.e. the sweep angle is large. Mean velocities, turbulence statistics, wall shear stress and instantaneous flow structures are investigated. Particular attention is devoted to the statistics of the shear stress on the walls of the channel and the wire in the recirculation zone. The flow around the mean reattachment region, at the termination of the recirculating bubble, does not exhibit the typical decay of the mean shear stress observed in classical backward-facing step flows owing to the presence of a strong axial flow. The evolution of the mean wall shear stress angle after reattachment indicates that the flow recovers towards equilibrium at a rather slow rate, which decreases with sweep angle. Finally, the database is analysed to estimate resolution requirements, in particular around the recirculation zones, for large-eddy simulations. This has implications in more complete geometrical models of a wire-wrapped assembly, involving hundreds of fuel pins, where only turbulence modelling can be afforded computationally.

1. Introduction

Studies of heat transfer in turbulent flows with separation, in particular recirculating flows, have a long history (Kays & Crawford 2004). Understanding the statistics of these flows, which influence reattachment length and internal structure of the recirculation bubble, and the properties of the small-scale turbulence is of fundamental interest. Separation in turbulent flows can be caused, for example, by geometrical complexity or an adverse pressure gradient. These flows include flow separation, shear layers, reattachment and the recovery of non-equilibrium turbulence towards equilibrium downstream of the reattachment point. Each of these phenomena has a distinct character and shows a high degree of variability between cases. Still one can

† Email address for correspondence: rranjan2@illinois.edu

classify such turbulent flows into two categories, namely, those with separation and those with turbulence-induced secondary flows. Different features of two- and three-dimensional turbulent boundary layer separation are reviewed in detail by Simpson (1996).

In this paper, we investigate the turbulent flow in a channel with a circular wire placed on one of the walls using direct numerical simulation (DNS). In particular, the mean flow has velocity components in the axial direction of the wire and perpendicular to it. This crossflow scenario has not been exhaustively investigated in the past, although it represents a first-order geometrical simplification of turbulent flows along complex wire-wrapped assemblies utilized in some nuclear reactors. The purpose of this configuration is to enhance mass transfer, heat transfer and mixing in several industrial and chemical processes. In the presence of crossflow, the recirculation bubble behind the wire is not closed in the mean since axial flow is also present. A review of DNS as a research tool to simulate turbulent flows is provided by Moin & Mahesh (1998) and a discussion of applicability of DNS to complex flows is provided by Karniadakis (1999). Some examples of recent simulations of turbulent flows in complex geometries include the DNS of turbulent flow in a stationary and serpentine passage by Laskowski & Durbin (2007), of a round turbulent jet in a laminar crossflow by Muppidi & Mahesh (2007) and flow through low-pressure turbine cascades by Rodi (2006).

The canonical flows exhibiting recirculation features include flow over a backward-facing step, forward-facing step, surface-mounted rib, bump on a surface, half cylinder and channel with a constriction. A frequently studied flow is the backward-facing step flow where a separation bubble exists owing to an abrupt geometry change. Backward-facing step flow has been studied in great detail in the past due to its geometrical simplicity (Bradshaw & Wong 1972; Eaton & Johnston 1981). A key feature of this flow is the slow boundary layer recovery after reattachment and an important characteristic is the reattachment length of the primary separation bubble (Bradshaw & Wong 1972; Eaton & Johnston 1981; Simpson 1996). For a given step size the reattachment length increases in the laminar regime as the Reynolds number is increased. It decreases in the transitional regime when Reynolds number is increased and then remains nearly Reynolds number independent in the turbulent regime (Armaly *et al.* 1983). Numerous studies of this flow have been reported (e.g. Adams & Johnston 1988; Shih & Ho 1994; Le, Moin & Kim 1997; Kaiktsis & Monkewitz 2003; Dejoan & Leschziner 2004; Sheu & Rani 2006; Rani, Sheu & Tsai 2007). Flow over forward-facing step has also received considerable attention (Farabee & Casarella 1986; Wilhelm, Härtel & Kleiser 2003; Camussi *et al.* 2008). This flow develops two recirculating regions, one upstream of the step and another downstream of the step. This flow also shows slow recovery of the boundary layer after reattachment.

More complex flows include turbulent flow past a surface mounted two-dimensional rib (Acharya *et al.* 1994; Hwang, Chow & Peng 1999; Liua, Ke & Sung 2008) and over curved walls (Wu & Squires 1998; Marquillie & Ehrenstein 2003; Mittal, Simmons & Najjar 2003; Gallaire, Marquillie & Ehrenstein 2007; Griffith *et al.* 2007). Marquillie, Laval & Dolganov (2008) performed a DNS study of channel flow with one smooth curved surface and found that the separated regime is characterized by disappearance of the low-speed streaks, which reappear further downstream after reattachment. The beginning of the separation bubble is characterized by low levels of turbulence kinetic energy compared to the downstream part of the bubble where small vortices interact

with large structures convecting into the boundary layer. In other studies, recirculation regions are produced by enforcing adverse pressure gradients. These flows are devoid of curvature effects and isolate phenomena associated with the separation of the flow (Wood & Bradshaw 1982; Kiya & Sasaki 1985; Dianat & Castro 1991; Honkan & Andreopoulos 1997; Spalart & Coleman 1997; Na & Moin 1998; Spalart & Strelets 2000; Caruelle & Ducros 2003; Angele & Muhammad-Klingmann 2006; Deck & Thorigny 2007; Sadeque, Rajaratnam & Loewen 2008). The common theme that has emerged in the study of these flows is that curvature, adverse or favourable pressure gradients and impingement of the shear layers on the walls affect in an important manner the overall flow dynamics and mean turbulence quantities. All these effects are present in the flow considered in this study in addition to the effect associated with the presence of a crossflow component.

Fewer studies have concentrated on separation bubbles with a crossflow component. In this case, the separation bubble is not closed because of the simultaneous presence of streamwise and spanwise mean flow component. Similar to many turbulent flows, the linear relationships between the Reynolds stresses and the strain rate tensor do not hold away from the wall in swept turbulent boundary layer flows over forward-facing steps (Johnston 1970; Bradshaw 1987; Webster, DeGraaff & Eaton 1996). Weber & Danberg (1992) performed experimental measurements of the mean velocity in flow over a swept backward-facing step and found that the boundary layer thickness increases with an increase in the sweep angle. Kaltenbach & Janke (2000) performed DNS of flow separation behind a swept rearward-facing step by varying the sweep angle between 0° and 60° and found that the reattachment length is reduced up to 50 % for high sweep angles. Kaltenbach (2003) performed a DNS of the flow behind a swept backward-facing step to study the effect of skewing on the turbulence properties and found that strain-induced stretching, compression and skewing of the mean flow influences the turbulence properties only in the vicinity of separation. In these studies, the sweep angle was varied from 0° to 60°.

Unfortunately, little is known about flows with large sweep angles, which could be considered on their own right more appropriately as turbulent crossflows. This is the main objective of the present study, where the bulk crossflow velocity is varied between 0 % and approximately 32 %, of the bulk axial velocity, or between 72° and 90° in terms of the sweep angle. The crossflow angle is defined as the angle formed by the net bulk velocity with the axial direction and the sweep angle is defined as the angle formed by the net bulk velocity with the crossflow direction. One noticeable difference between these flows and other backward-facing step flows is that the flow within the recirculation region is always fully turbulent, owing to the presence of a large axial flow. The objective of the present study is to understand the nature of the mean flow, obtain turbulence statistics, analyse the shear stress distribution and instantaneous flow structures around the region of recirculation and to derive quantitative estimates of the grid resolution requirements in coarser numerical-modelling representations. Real wire-wrapped assemblies are too complex to be accessible using DNS. They usually consist of hundreds of nuclear fuel pins with associated wires wrapped helically around them. The configuration studied here corresponds to an average situation in the real assembly. Moreover, given the complexity of this geometry, the engineering design and optimization of the assembly is forced to employ modelling, e.g. large-eddy simulation (LES) or Reynolds averaged Navier–Stokes (RANS), where the present results can be valuable for comparisons and validation.

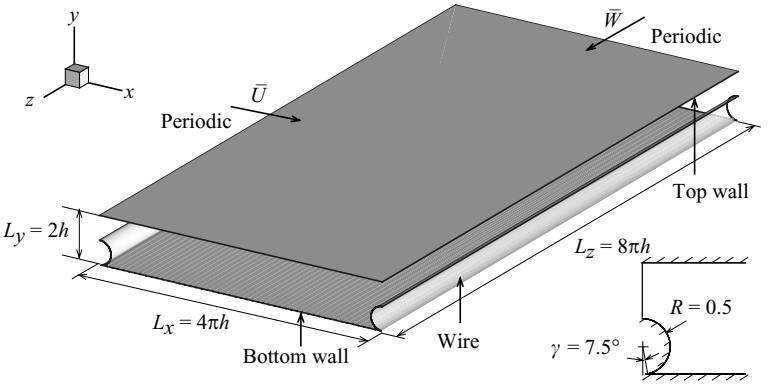

FIGURE 1. Schematic of the geometry considered in the present study.

2. Flow description

The problem considered in this study corresponds to a channel with a wire placed on the bottom wall of the channel. A schematic of the problem is shown in the figure 1. The domain size is $L_x \times L_y \times L_z = 4\pi h \times 2h \times 8\pi h$ in the x, y and z directions, respectively. The x coordinate denotes the crossflow direction, y is the vertical direction and z is the streamwise or axial direction. The streamwise and crossflow directions are considered to be periodic. For convenience, the centre of the cylindrical wire of radius $R = 0.5h$ is placed at the boundary of the periodic domain. Previous studies of flows in periodic channels with hills by Mellen, Fröhlich & Rodi (2000), Fröhlich *et al.* (2005) and Peller & Manhart (2006) suggest that good streamwise decorrelation and complete flow reattachment is observed using streamwise periodic boundary conditions if $L_x \geqslant \pi h_o$, where h_o denotes the hill (obstacle) height. Therefore, in the present study, the crossflow length of the domain was chosen as $L_x = 4\pi h$.

In practical wire-wrapped assemblies, the wire is wrapped under tension around a nuclear fuel pin and there is a slight deformation of the wire at the contact location. To approximately model this detail we have chosen to impose a finite contact angle between the wire and the wall. Therefore, the contact half-angle of the wire with the bottom wall of the channel is $\gamma = 7.5°$ (see right-bottom inset in figure 1). The flow in the channel is driven by the pressure gradient resulting from the imposed constant flowrates along the axial and crossflow directions. In this study, the flowrate specified in the axial direction is higher than that imposed in the crossflow direction. The resulting crossflow over the wire produces a large recirculation region or bubble with mean axial flow, in the lee side of the wire. The crossflow detaches from the top surface of the wire, a shear layer is formed over the recirculation zone, and the flow then finally reattaches some distance downwind from the wire.

3. Mathematical formulation, approach and parameters

3.1. *Governing equations and numerical method*

The motion of an incompressible fluid with constant density ρ, and viscosity μ is governed by the Navier–Stokes equations,

$$\rho\left(\frac{\partial \boldsymbol{u}}{\partial t} + \boldsymbol{N}(\boldsymbol{u})\right) = -\nabla p + \mu\nabla^2\boldsymbol{u}, \tag{3.1}$$

and the continuity equation

$$\nabla \cdot \boldsymbol{u} = 0, \tag{3.2}$$

in the computational domain Ω, where $\boldsymbol{u} \equiv (u, v, w)$ represents the velocity field and p is the pressure. The term $\boldsymbol{N}(\boldsymbol{u})$ represents the nonlinear advection term, given by

$$\boldsymbol{N}(\boldsymbol{u}) = \frac{1}{2}[(\boldsymbol{u} \cdot \nabla)\boldsymbol{u} + \nabla \cdot (\boldsymbol{u}\boldsymbol{u})]. \tag{3.3}$$

This particular skew-symmetric form of $\boldsymbol{N}(\boldsymbol{u})$ has been shown by Zang (1991) to be more robust compared to other forms that are equivalent in the continuous case, e.g. convective and rotational forms, when the governing equations are discretized. In particular, this form minimizes aliasing errors of the spatial discretization used in this study. Periodic boundary conditions are employed along the axial and crossflow directions and the no-slip boundary condition is used at the walls and at the surface of the wire. The mean flow, with axial and crossflow components, is maintained by a constant pressure-gradient forcing imposed along these directions.

Time dependent simulations based on the above set of equations are carried out using a spectral element method implemented in *Prism* (Henderson 1994). The equations are discretized using two-dimensional spectral elements in the x–y plane and Fourier modes in the axial direction. In the spectral element method, the domain Ω is subdivided into K macro elements. Within each of these elements the geometry and the solution variables are represented by using Nth-order tensor-product polynomial expansions as basis functions. These basis functions are Gauss–Lobatto–Legendre (GLL) polynomial interpolants. A third-order accurate time-splitting scheme developed in Karniadakis, Israeli & Orszag (1991) is used to integrate the above set of equations. The splitting scheme leads to a set of equations comprising of an advection equation, and a sequence of elliptic Helmholtz equations enforcing the incompressibility constraint and the linear viscous term present in the semi-implicit time integration. The advection terms are treated explicitly in this approach while the system of implicit elliptic Helmholtz equations are solved by a direct method using static condensation. Henderson & Karniadakis (1995) provides more details of the method and the solution strategy.

3.2. *Simulation parameters*

All statistical quantities in the flow studied here depend on the x and y coordinates. The z- and time-averaged mean of a flow quantity $\phi(x, y, z, t)$ is denoted by $\langle\phi\rangle$ and is defined as follows,

$$\langle\phi\rangle(x, y) = \frac{1}{N}\sum_{i=1}^{N}\left(\frac{1}{L_z}\int_0^{L_z}\phi(x, y, z, t_i)\,\mathrm{d}z\right), \tag{3.4}$$

where L_z is the length of the domain in the homogeneous axial direction, i denotes a time index and N is the total number of instants used to compute the time average. These running averages are determined only after the simulations reach a statistically steady state, as discussed below. The flowrates are defined in the customary manner, according to

$$Q_z = \iint_S W(x, y)\,\mathrm{d}x\,\mathrm{d}y, \tag{3.5}$$

where S denotes the x–y cross-section of the domain and

$$Q_x = L_z \int U(x, y)\,\mathrm{d}y, \tag{3.6}$$

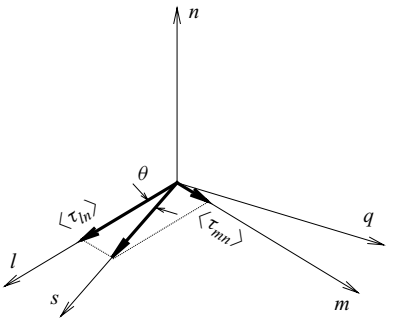

FIGURE 2. Wall shear stress coordinate system. Thick solid lines denote components of wall shear stress on l-, s- and m-axis, respectively.

with $\langle u \rangle = U$ and $\langle w \rangle = W$ denoting the average crossflow and streamwise velocity component, respectively. Note that (3.6) is independent of x when the flow is statistically stationary, according to the continuity equation (3.2). In the present problem, mean flow occurs in both axial as well as crossflow directions. This is similar to three-dimensional turbulent boundary layers with crossflow inhomogeneity. This leads to the presence of a net mean flow direction which can be defined in terms of wall shear stress components (Simpson 1996). The components of the shear stress tensor $\boldsymbol{\tau}$ are defined by

$$\tau_{ij} = \mu \left(\frac{\partial u_i}{\partial x_j} + \frac{\partial u_j}{\partial x_i} \right). \tag{3.7}$$

The traction T_i on the wall surface is given by

$$T_i = \tau_{ij} n_j, \tag{3.8}$$

where $\boldsymbol{n} = \{n_j\}$ represents the normal to the wall surface. The traction can then be projected along a new right-handed coordinate system with direction vectors $\boldsymbol{m}$, $\boldsymbol{n}$ and $\boldsymbol{l}$. On the walls of the channel, $\boldsymbol{m}$, $\boldsymbol{n}$ and $\boldsymbol{l}$ are aligned with the x-, y- and z-axis, respectively. On the surface of the wire, $\boldsymbol{l}$ is aligned with the z-axis, m is aligned with the azimuthal direction and n is aligned with the radial direction. The corresponding components of traction or wall shear stresses in the streamwise and crossflow directions, τ_{ln} and τ_{mn} respectively, are given by

$$\tau_{ln} = T_i l_i, \tag{3.9}$$

$$\tau_{mn} = T_i m_i. \tag{3.10}$$

The angle formed between the mean streamwise and crossflow wall shear stresses is defined as the local net flow direction, given by

$$\theta = \tan^{-1} \left(\frac{\langle \tau_{mn} \rangle}{\langle \tau_{ln} \rangle} \right), \tag{3.11}$$

where $\langle \tau_{mn} \rangle$ and $\langle \tau_{ln} \rangle$ denote the mean wall shear stresses. A new orthogonal coordinate system (s–q–n) can be obtained by rotating the (l–m–n) system about the n-axis (Simpson 1996). The sketch of the coordinate systems is shown in figure 2. The new s coordinate is along the direction defined by θ, while q is oriented perpendicular to n and s. Under some circumstances, it is possible that a semi-log composite relationship may exist for the mean velocity profile along this direction. Simpson (1996) has shown that the wall shear stress vector is also aligned closely with the

wall-parallel turbulent shear stress vector close to the wall; not generally aligned with the strain rate vector (Johnston 1970; Bradshaw 1987; Webster *et al.* 1996), an assumption built into linear eddy-viscosity models. The net mean flow along direction s in the new system is given by

$$V_s = \langle w \rangle \cos\theta + \langle u \rangle \sin\theta. \tag{3.12}$$

The flow is characterized by employing the bulk axial velocity, $W_b = Q_z/S$, and the channel half height h as the characteristic velocity and length scales, respectively. These characteristic scales are used to define the Reynolds number in the axial direction, given by

$$Re_z = \frac{\rho W_b h}{\mu}. \tag{3.13}$$

The Reynolds number in the crossflow direction is defined by

$$Re_x = \frac{\rho U_b h}{\mu}, \tag{3.14}$$

where $U_b = Q_x/(2hL_z)$ is the bulk velocity in the crossflow direction. The crossflow angle θ_c is defined as

$$\theta_c = \tan^{-1}\left(\frac{U_b}{W_b}\right), \tag{3.15}$$

and the sweep angle θ_w is defined as

$$\theta_w = \tan^{-1}\left(\frac{W_b}{U_b}\right). \tag{3.16}$$

The bulk Reynolds number is defined as

$$Re_b = \sqrt{Re_x^2 + Re_z^2}, \tag{3.17}$$

and the friction Reynolds number is given by

$$Re_\tau = \frac{\rho u_\tau h}{\mu}, \tag{3.18}$$

where

$$u_\tau = \sqrt{\frac{\overline{\tau}_w}{\rho}}, \tag{3.19}$$

is the friction velocity and $\overline{\tau}_w$ is the overall average shear stress at all the walls (see (3.21)). Owing to the presence of the wire and its induced secondary flows, a local average wall shear stress can be defined along direction s, similar to Simpson (1996) and Kaltenbach (2003), given by

$$\tau_w = \langle \tau_{ln} \rangle \cos\theta + \langle \tau_{mn} \rangle \sin\theta. \tag{3.20}$$

This is also the maximum average shear stress on the wall at any particular location. The overall average shear stress used in (3.19) is given by

$$\overline{\tau}_w = \frac{1}{S_{top} + S_{bot}}\left(\iint_{S_{top}} \tau_w \, \mathrm{d}S + \iint_{S_{bot}} \tau_w \, \mathrm{d}S\right), \tag{3.21}$$

where S_{bot} and S_{top} denote the surface of the bottom wall including the wire and the top wall, respectively. In most figures, the wall-shear stress is non-dimensionalized using

Case	Re_z	Re_x	Re_b	Re_τ	Q_z	Q_x
A	5400	0	5400	305	21.94	0
B	5400	417	5416	307	21.94	3.49
C	5400	842	5465	312	21.94	7.05
D	5400	1709	5664	335	21.94	14.32

TABLE 1. Simulation parameters for all cases.

a characteristic shear stress based on the viscous scaling, $\tau_c = \mu W_b / h$. Alternatively, the non-dimensionalization of the wall-shear stress can use an inertial scaling, which leads to the definition of the skin-friction coefficient C_f, given by

$$C_f = \frac{\tau_w}{\frac{1}{2}\rho W_b^2}. \tag{3.22}$$

The results for the wall-shear stress τ_w in this study are non-dimensionalized by τ_c. However, the value of C_f can be obtained using the following relation,

$$C_f = \frac{2}{Re_z}\left(\frac{\tau_w}{\tau_c}\right). \tag{3.23}$$

Four simulations, labelled A through D, are investigated in this study with identical flowrate in the axial direction and varying flowrates in the crossflow direction. The first simulation, Case A, has no crossflow over the wire and is considered as a reference scenario to compare with the other cases with crossflow, where recirculation bubbles are present. The crossflow rate is increased, from cases B to D, to investigate the effect of the wire and the amount of crossflow on the overall flow behaviour. Table 1 lists some of the parameters of these simulations, including all the Reynolds numbers defined above. Case A has no crossflow whereas the other cases have increasing amounts of crossflow. The initial flow field of Case A is generated by imposing harmonic perturbations of 20 % intensity over a parabolic velocity profile of the specified flowrate. The flow evolves until a fully developed and statistically stationary turbulent state is reached. This is verified by monitoring that the first- and second-order statistics as well as the wall-averaged shear stress ceases to change with time. The fully developed flow for Case A is then used as the initial condition for Case B. The initial flow field of Case B evolves again through a transient period until it reaches a statistical stationary state. Proceeding in similar fashion, the initial flow fields for cases C and D are obtained from the fully developed flow fields of cases B and C, respectively. Turbulence statistics were gathered after the initial transients had subsided. The statistics for Case A, the slowest case to converge, are gathered for approximately 15 mean flow through times. The time intervals for the other cases were slightly shorter. The flow through time is based on the bulk axial velocity, W_b, and the extent of the channel in the axial direction, L_z. The case with the largest crossflow, D, shows faster approach towards statistical convergence compared to other cases.

3.3. *Computational grid*

The computational mesh comprises of macro spectral elements where each element is resolved by a high-order polynomial basis function. The mesh conforms to the boundary shape to enhance accuracy and improve convergence. The macro spectral elements were created using an elliptic grid generation technique (implemented in MATLAB using an unstructured triangular mesh). The elements at the corners

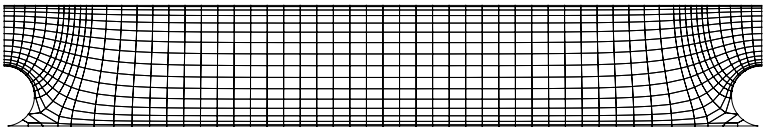

FIGURE 3. Macro spectral elements in the x–y plane.

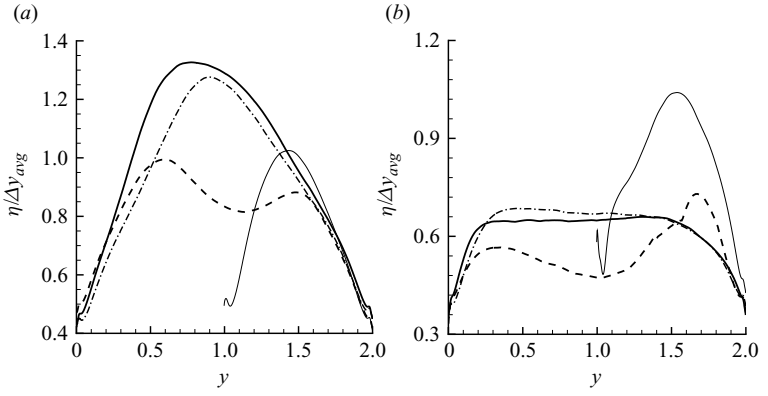

FIGURE 4. Profiles of η normalized by Δy_{avg} for cases B (a) and D (b) at different crossflow locations. Thin solid, thick dashed, thick solid and thin dashed-dotted curves denote the top of the wire, centre of primary separated bubble, mean reattachment location and centre of the channel, respectively.

regions, where the wire contacts the wall, were modified manually to improve their quality. The resulting final mesh is shown in figure 3. After a few trials, a mesh containing a total of 936 macro elements in the x–y plane was selected. Each of these elements are further resolved by a 15th-order GLL polynomial. A total of 512 Fourier modes are used in the homogeneous z direction, resulting in an overall 107 827 200 collocation points. This mesh was found to be sufficiently accurate to resolve all the scales of the flows considered in this study. This was verified by determining the inner-scaled mesh spacing using the axial flow velocity, which is constant in all simulations. A non-uniform wall-normal spacing of the elements is used to ensure higher density of mesh points close to the walls. The first mesh point away from the wall is located at $y^+ \approx 0.13$ and maximum spacing at the centreline of the channel is 4.3 wall units. At all the locations on the channel wall and the wire surface there are 15 or more collocation points below $y^+ = 10$. A non-uniform spacing is also used in the x direction with a minimum grid spacing of $\Delta x^+ \approx 2$ close to the wire and a maximum grid spacing of $\Delta x^+ \approx 6$ in the centre of the domain. Apart from the inner-scaled mesh spacing, the Kolmogorov length scale, $\eta = (\nu^3/\epsilon)^{1/4}$ (where $\nu = \mu/\rho$ and ϵ denote the turbulence dissipation), is extracted from the simulations. The profiles of η normalized by $\Delta y_{avg} = 1/2(\Delta y_{min} + \Delta y_{max})$ for cases B and D are shown in figure 4 at four different representative crossflow locations. These crossflow locations will be discussed later in § 5. A resolved simulation usually requires at least

$$\kappa_{max}\eta \gtrapprox 1, \quad \text{then} \quad \frac{\eta}{\Delta y_{avg}} \gtrapprox \frac{1}{\pi}, \tag{3.24}$$

where κ_{max} denotes the highest resolved wavenumber (Pope 2000). Figure 4 shows that the above requirement is satisfied at all considered crossflow locations, which indicates

that the grid resolution is sufficient. In particular, since Case D appears adequately resolved and since the dissipative length scale is proportional to the inverse of the Reynolds number, the other lower Reynolds number cases (A, B and C) are likely also well resolved.

4. Instantaneous flow structures

A recirculation bubble is characterized by the presence of a shear layer roll up near the separation zone and three-dimensional structures near its reattachment point (Eaton & Johnston 1981; Chun & Sung 2003). An increase in shear-layer entrainment is associated with a decrease in the reattachment length owing to a balance between pressure-driven backflow and re-entrainment by the separated shear layer (Adams & Johnston 1988). It has been observed in backward-facing step flows that turbulence is far from equilibrium near the reattachment zone owing to impingement of vortical structures, emanating from the shear layer, on the wall (Song & Eaton 2004). Thus, instantaneous flow structures reveal physical aspects of the flow, e.g. separation, reattachment and recovery, and they are used commonly to analyse flows.

The λ_2-vortex criterion of Jeong & Hussain (1995) is adopted here in order to investigate some of the instantaneous small-scale structures observed in the flow. This criterion identifies a vortex core defined as a region having net vorticity and simultaneously excluding regions of potential flow. Using this criterion, vortical structures present in the near-wall regions for cases A and C are obtained and are shown in figures 5 and 6, respectively. The structures observed in cases B and D are qualitatively similar to those shown in Case C below and, therefore, they are not shown.

The instantaneous flow visualization in figure 5, shows elongated quasi-streamwise vortices around the near-wall regions, at both the flat channel walls and the wire surface. These streamwise vortices in the near-wall region are similar to those observed in the wall region of turbulent boundary layers (Rajagopalan & Antonia 1993). The streamwise extent of these vortices is approximately 200–300 wall units. These quasi-streamwise vortices appear to be overlapping in the streamwise direction as a result of their mutual interaction. These overlapping vortices form chain-like regions as seen in the encircled regions in figure 5. The streamwise extent of these chain-like regions is about 800–900 wall units. These structures tend to have positive and negative tilt, with respect to the axial direction, and are inclined at small angles with respect to the vertical direction. The present observations are consistent with previous visualizations in turbulent channel flows (Jeong *et al.* 1997).

Figure 6 shows the vortical structures for Case C in the near-wall region and the recirculation zone. Away from the recirculation zone, where the flow is attached, quasi-streamwise vortices are observed which have similar features as the streamwise vortices in turbulent channel flows, boundary layers and Case A. The streamwise extent of these vortices is approximately 130–300 wall units. Additionally, the complete flow separation from the top of the wire produces a shear layer with intense vortical structures having no preferential orientation. Near the reattachment zone the worm-like vortices get distorted due to mean flow straining (Song & Eaton 2004). This is followed by recovery towards the boundary layer behaviour, with vortical structures oriented along the quasi-streamwise direction (Le *et al.* 1997; Lee & Sung 2002). Similar to Kaltenbach (2003), downstream of the reattachment zone, densely packed structures exist consisting of entangled filaments with a preferential orientation aligned with the mean flow. Streamwise vortices with a maximum streamwise extent of about

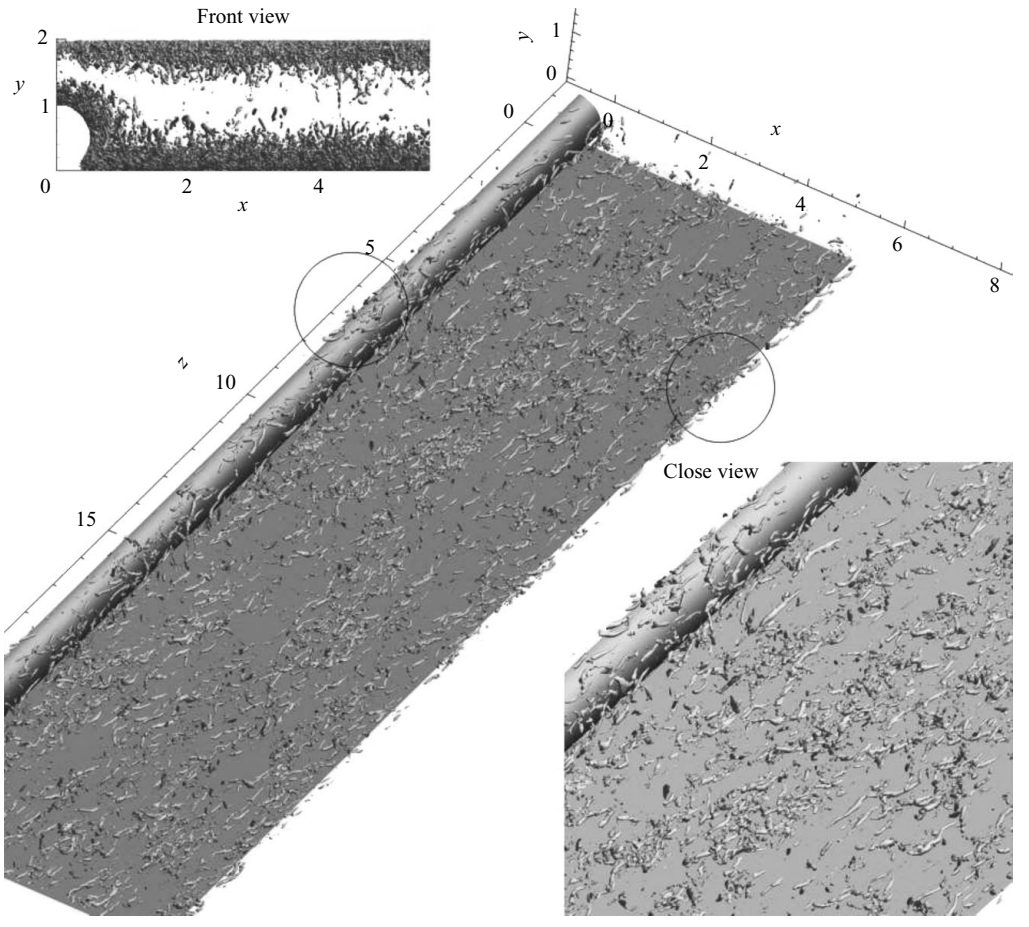

FIGURE 5. Vortical structures in the near-wall region for Case A identified by $W_b^2\lambda_2/h^2 = -4$. The encircled region contains representative chain-like regions.

400 wall units are also present near the wire top surface. These structures loose their streamwise orientation once the flow detaches to form the shear layer.

The vorticity vector is closely associated with the orientation of the vortical structures (e.g. Honkan & Andreopoulos 1997). Figure 7 shows the effect of crossflow on the orientation of these vortical structures by inspecting the iso-surfaces of axial vorticity ω_z normalized by W_b/h, in the near-wall region and in the shear-layer region for cases C and D. Structures with negative axial vorticity, in the near-wall region have a negative tilt with respect to the axial direction for both cases. This is similar to the behaviour observed in turbulent channel flows by Jeong *et al.* (1997), where a one-to-one correspondence was observed between negative vorticity having negative tilt and positive vorticity having a positive tilt with the streamwise direction in the near-wall region. The iso-surface of positive axial vorticity (not shown here) shows a positive tilt with respect to the mean flow direction. However, the vorticity does not show a specific orientation in the shear-layer region. This is a characteristic that is often encountered in free-shear flows. As the amount of crossflow is increased the overall magnitude of the vorticity increases in both the near-wall region as well

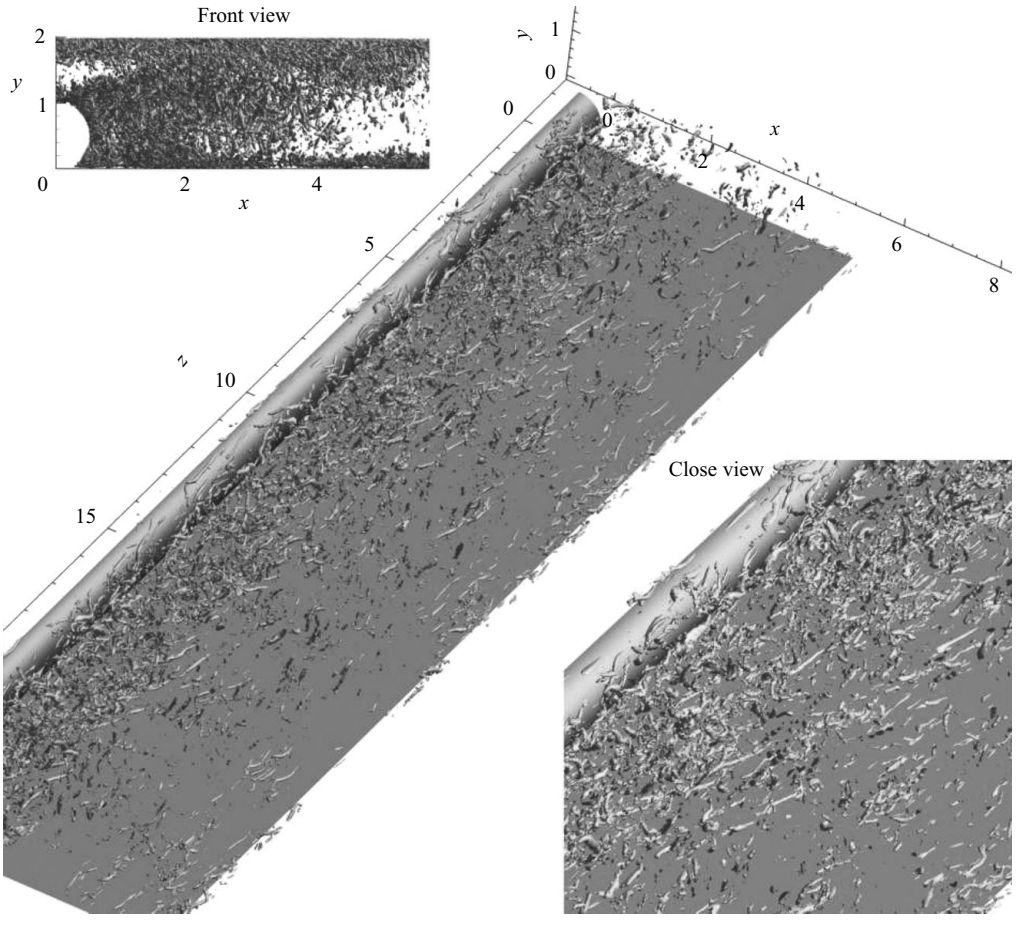

FIGURE 6. Vortical structures in the near-wall and recirculation regions for Case C identified by $W_b^2\lambda_2/h^2 = -4$.

as in the shear-layer region. Qualitatively, the orientation of the structures in the shear-layer and near-wall regions appear similar.

5. Turbulence statistics

Mean velocity profiles are investigated first, both in the original coordinates and in the inner-scaled shear stress coordinate frame. This is followed by a discussion of the behaviour of turbulence intensities at particular planes across the flow.

5.1. *Mean flow analysis*

Iso-contours of the mean axial velocity W, normalized by W_b, are shown in figure 8 for all cases. In Case A, without crossflow, the velocity in the centre of the channel is similar to that of a turbulent channel flow. As expected, symmetry is observed about the mid-plane because of the inherent symmetry of the boundary conditions. The effect of the wire is felt up to approximately two wire diameters measured from the side boundaries of the computational domain. In this region, there is a decrease in the vertical velocity gradient near the walls. In the cases with crossflow, a region of

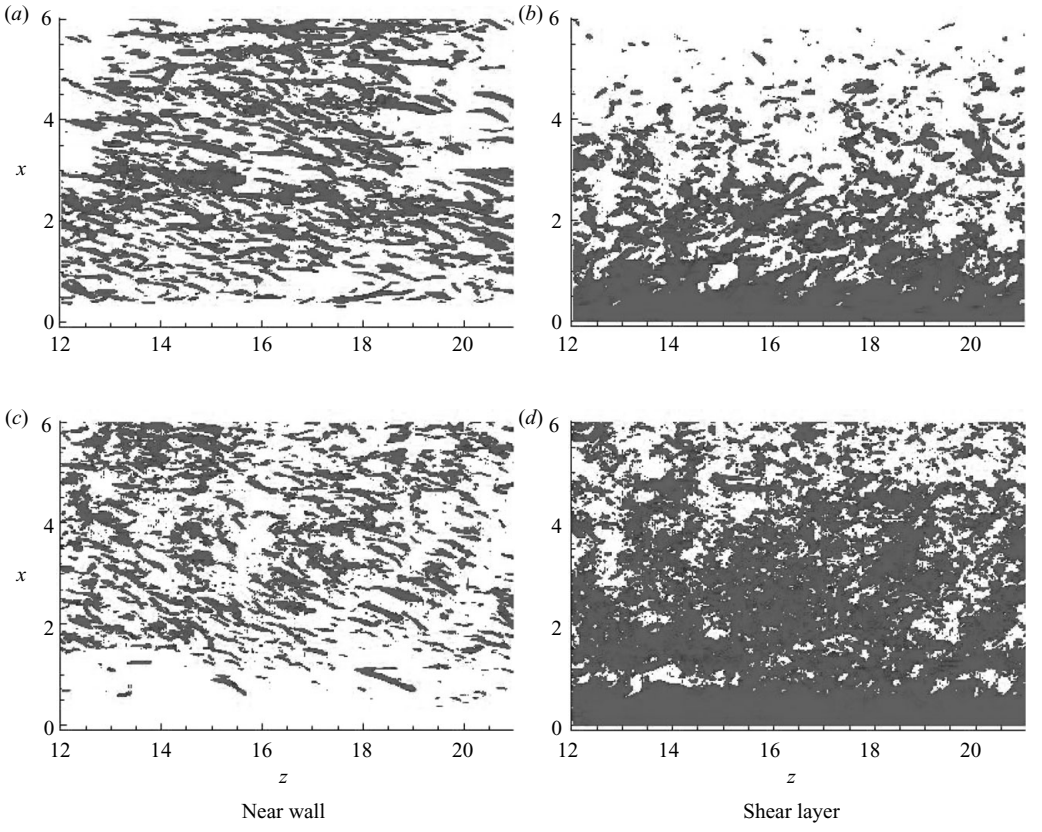

FIGURE 7. Iso-surface of the non-dimensionalized axial vorticity, $h\omega_z/W_b = -3.33$, for Case C (a, b) and $h\omega_z/W_b = -5.55$, for Case D (c, d), in the near-wall region with y^+ ranging from 15 to 60 (a, c) and in the shear-layer region with y^+ ranging from 160 to 370 (b, d).

detached flow forming a recirculation bubble adjacent to the wire is observed. This detached-flow zone is created by the imposed crossflow.

Qualitatively, the flow can be classified into four general regions, namely: the recirculation bubbles, the shear layer, the attached flow region in the centre of the channel and the acceleration region in the windward side of the wire. Iso-contours of the mean crossflow velocity U, normalized by W_b, and a projection of the mean streamlines in the x–y plane are shown in figure 9. Results for Case A are not shown because U is very small in this simulation and there is no recirculation zone. In all other cases, the flow separates near the top of the wire and forms two clear recirculation bubbles in the leeward side of the wire. These bubbles will be referred as the primary and the secondary bubbles from here onwards. The primary bubble is larger than the secondary bubble, as their naming implies. The size of both bubbles increases with increasing crossflow velocity. High-velocity gradients occur at the top of the wire and a shear layer is formed. After reattachment, the flow recovers towards the centre of the channel. When the flow reaches the windward side of the wire, it starts accelerating owing to the reduction in cross-sectional area. The rapid geometric constriction also causes the flow to separate leading to the formation of another recirculation bubble close to the wire. The size of this bubble remains similar in all the cases with crossflow.

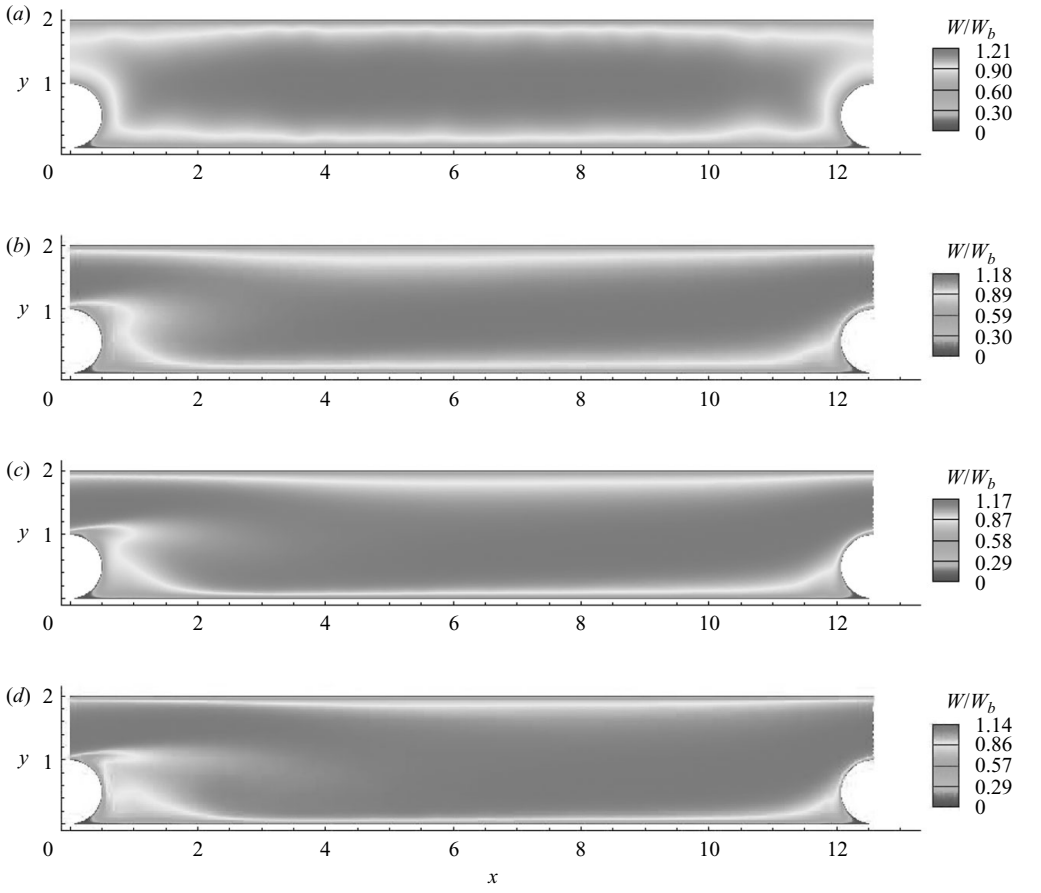

FIGURE 8. Iso-contours of mean axial velocity normalized by W_b for cases A (*a*), B (*b*), C (*c*) and D (*d*).

In the present simulations for the particular geometry under consideration and the chosen flow parameters the adverse pressure gradient downstream of the wire on the top wall is too small for the flow to separate from the top wall. It is observed in figure 9 that the streamlines near the upper wall are deflected away from the wall but the pressure gradient is insufficient to induce flow separation. For example, separation from the top wall was observed in previous studies with flow over backward-facing steps (Armaly *et al.* 1983; Shih & Ho 1994) and on the wall facing a constriction in a channel (Mittal *et al.* 2003).

A three-dimensional rendering of selected mean flow streamlines for Case C is shown in figure 10. Since the flow is periodic in the z direction, it is possible to chose an arbitrarily large streamwise domain length for the purpose of plotting mean streamlines. The extent of the domain in figure 10 is $1.25L_z$, so that the spiral nature of the streamlines inside the separated bubble is apparent. The figure shows six streamlines in the vicinity of the wire where the recirculation zone is observed. The streamlines s_1 and s_2 emanate from regions above the primary bubble. These streamlines skip the bubble region and travel towards the attached flow region. The streamlines s_3, s_4, s_5 and s_6 are located within the primary bubble region. The rotational character of the flow is observed in these streamlines, where the spiralling

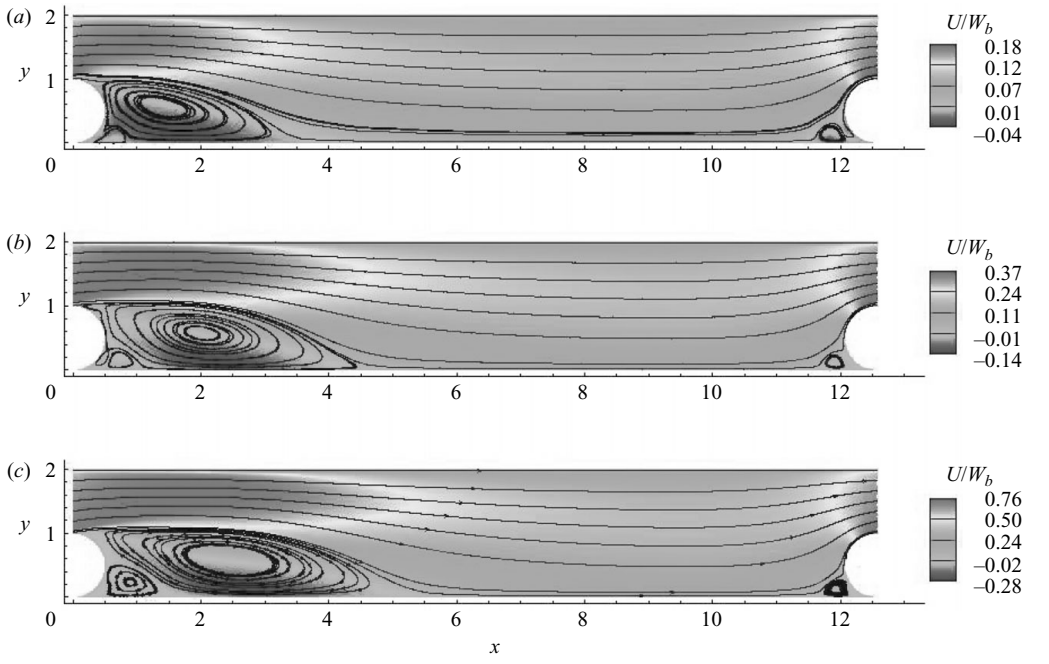

FIGURE 9. Iso-contours of mean crossflow velocity normalized by W_b and two-dimensional projection of the mean streamlines for cases B (*a*), C (*b*) and D (*c*).

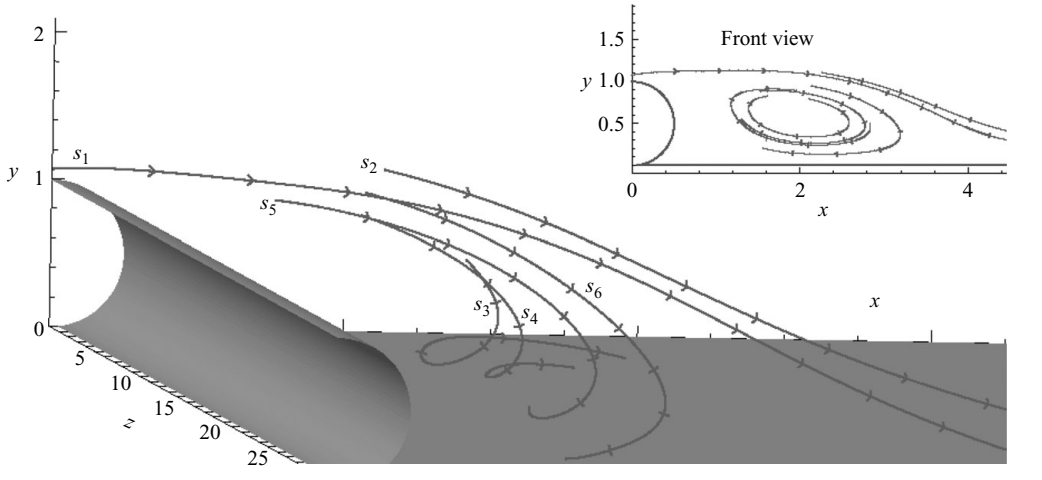

FIGURE 10. Three-dimensional rendering of selected mean streamlines for Case C.

behaviour is indicative of the interaction of the crossflow with the axial flow within the recirculation bubble. In the attached zone, the spiral nature is not observed as the velocity vector in the x–y plane does not reverse direction. This type of spiral or helical path has been observed previously, for example, by Kaltenbach & Janke (2000) in a study of flow behind a swept rearward-facing step and by Sheu & Rani (2006) in flow over a backward-facing step with sidewalls.

Velocity profiles in terms of friction-based, inner, coordinates along the vertical direction y at different crossflow locations are investigated next. The profiles are

	Spanwise locations			
Case	x_t/h	x_c/h	x_b/h	x_r/h
A	0	2π	–	–
B	0	2π	1.39	3.32
C	0	2π	2.01	4.67
D	0	2π	2.46	5.55

TABLE 2. Particular locations of interest along the crossflow direction.

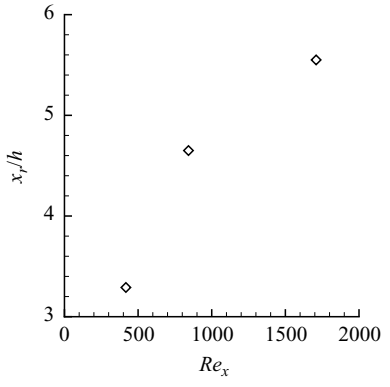

FIGURE 11. Variation of reattachment length with crossflow Reynolds number.

extracted at the locations denoted by x_t, x_c, x_b and x_r, corresponding to the top of the wire, centre of the channel, centre of primary recirculation zone and reattachment point, respectively. The reattachment location x_r is defined as the crossflow location where the shear stress $\langle \tau_{mn} \rangle$ changes sign. This is also the location of the mean dividing streamline based on mean crossflow and vertical velocity. Only the locations x_t and x_c are considered for Case A, since it has no recirculation zone. The locations where the profiles were extracted are summarized in table 2. Both x_b and x_r increase with increasing crossflow in the present simulations. The variation of the non-dimensional reattachment length, x_r/h, is shown in figure 11 in terms of crossflow Reynolds number Re_x. The reattachment length increases with Re_x, similar to backward-facing step flow (Armaly *et al.* 1983).

Profiles of the mean velocity component V_s (in the wall shear-stress frame) normalized by the friction velocity, $V_s^+ = V_s/u_\tau$, plotted against the vertical direction in the inner coordinate $y^+ = yu_\tau/\nu$ are provided in figure 12. The profiles have been extracted at each of the locations indicated previously for both, the bottom and top walls. The values of the friction velocity u_τ normalized by the bulk axial velocity W_b at the bottom and top walls at different crossflow locations are shown in table 3 for all the cases. In figure 12 the viscous sublayer relationship, $u^+ = y^+$ and the 'Law of the Wall' for a zero pressure gradient (ZPG) boundary layer, $u^+ = (1/0.4)\ \ln y^+ + 5.5$, are included. In the present study, the complexity of the flow is such that we did not attempt to incorporate pressure-gradient effects into a reference 'Law of the Wall' valid at each location (Nickels 2004), primarily because it is not *a priori* expected that equilibrium will be reached within the turbulent flow as it travels over the wire surface for such a law to be generally applicable here. The ZPG 'Law of the Wall'

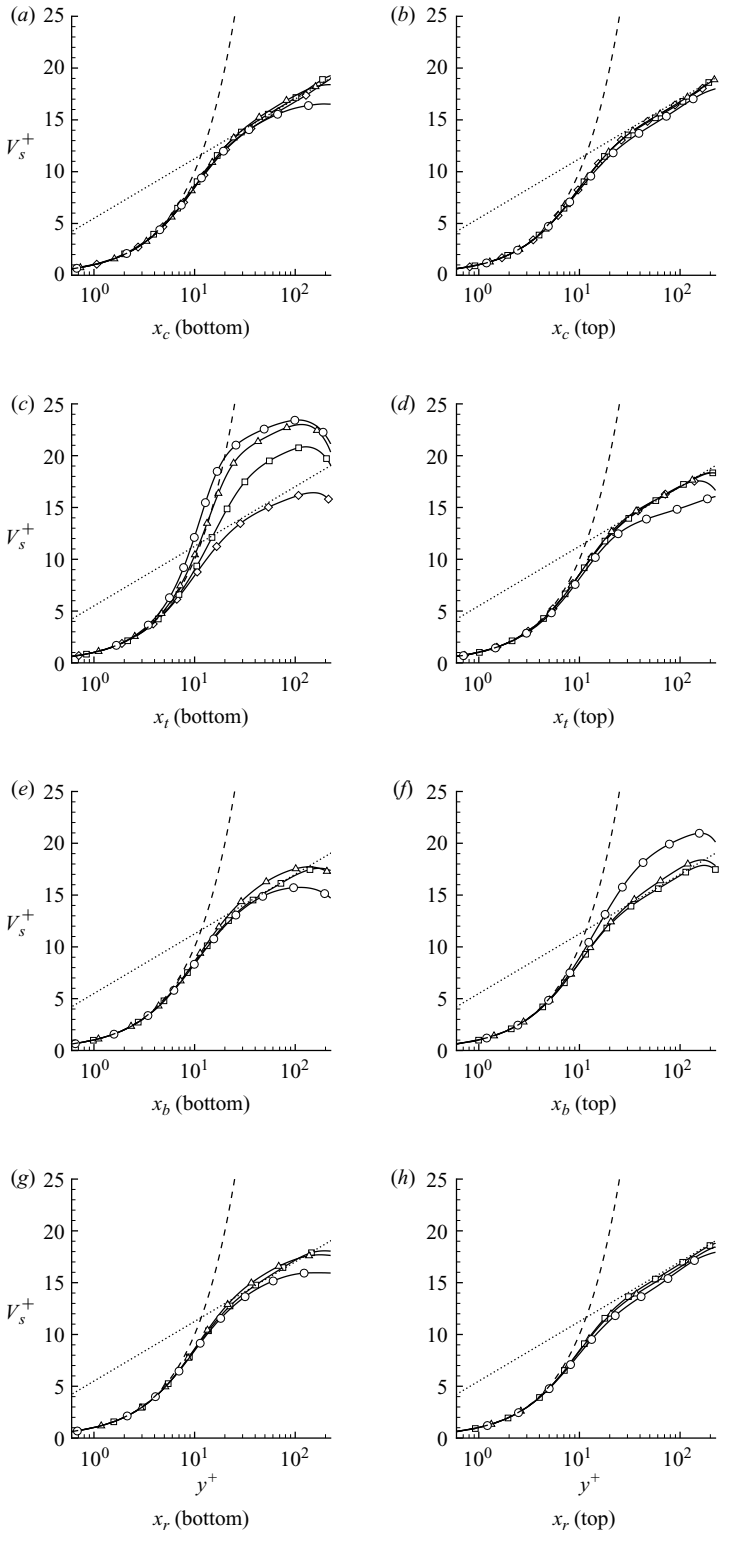

FIGURE 12. Profiles of mean velocity normalized with the friction velocity at different crossflow locations. Cases A, B, C and D are denoted with ◇, □, Δ and ○, respectively. Left and right subfigures show profiles from the bottom and top walls, respectively.

Case	Flow quantity	Spanwise locations			
		x_t/h	x_c/h	x_b/h	x_r/h
A	u_{τ_b}/W_b	0.058	0.061	–	–
	u_{τ_t}/W_b	0.054	0.061	–	–
B	u_{τ_b}/W_b	0.057	0.061	0.057	0.062
	u_{τ_t}/W_b	0.064	0.058	0.063	0.058
C	u_{τ_b}/W_b	0.052	0.063	0.060	0.064
	u_{τ_t}/W_b	0.065	0.058	0.064	0.060
D	u_{τ_b}/W_b	0.051	0.069	0.067	0.070
	u_{τ_t}/W_b	0.079	0.064	0.064	0.065

TABLE 3. Friction velocity normalized by W_b at different crossflow locations. Subscripts b and t denote values at bottom and top wall, respectively.

was considered solely as a means to establish a reference in the discussion of the profiles. The main interest of the following discussion is to investigate whether the inner-scaled velocity obeys a 'Law of the Wall', i.e. $V_s/u_\tau = F(y^+)$, and in the cases where it does, up to what distance above the wall is this approximation appropriate. This is motivated by practical needs to develop wall closure models in complex flows, e.g. wall-shear-stress models (Schumann 1975).

Figures 12(a) and 12(b) show the velocity profiles at location x_c, centre of the channel, from the bottom and top walls, respectively. All profiles, except at the highest crossflow rate, show good agreement with the ZPG law. The observed increasing deviations with increasing crossflow rate are caused by the growth of the main recirculation bubble. The reattachment point of the recirculation bubble moves closer to x_c as the crossflow rate increases, implying increasing non-equilibrium effects and more large scale vortices (Eaton & Johnston 1981; Simpson 1996; Le *et al.* 1997; Na & Moin 1998; Spalart & Strelets 2000; Liua *et al.* 2008). Figures 12(c) and 12(d) show the profiles at location x_t, top of the wire, measured from the bottom and top walls, respectively. For the cases with crossflow, the bottom wall velocity profiles deviate from the logarithmic law and exhibit higher log-region velocities but remain remarkably parallel to the logarithmic law; most of the deviation is therefore with respect to the slope intercept value. This is likely caused by the strong streamline curvature effects induced by the wire and favourable pressure gradient (FPG) present on the windward side (Webster *et al.* 1996). The profiles for all cases but Case D measured from the top wall follow the law of the wall. The profile for Case D shows a lower slope than the law of the wall in the log-layer region. This behaviour can not be modelled only by adjusting the slope intercept value since the von Kármán constant appears to change; provided a logarithmic law is assumed. Figures 12(e) and 12(f) show the profiles at location x_b, the centre of the main recirculation bubble, measured from the bottom and top walls, respectively. The profiles from the bottom wall deviates from the ZPG law. In particular, the bottom wall profiles of the cases with crossflow are not parallel to the law of the wall reference. The top wall profiles for all, but Case D, collapse approximately on the reference profile. The top wall profile for Case D overshoots the reference profile by a large amount, indicating that the flow is subjected to substantial FPG. In previous studies of backward-facing steps and similar flows, the velocity profile in the separation bubble does not exhibit

a logarithmic range owing to adverse pressure gradients (APG) (Dianat & Castro 1991; Kiel & Vieth 1995; Simpson 1996; Le *et al.* 1997; Na & Moin 1998; Spalart & Strelets 2000; Angele & Muhammad-Klingmann 2006). In the present case, there is an imposed axial flow, large sweep angle, and there is dominant turbulent wall-bounded flow in the z direction. Only in Case D, with the highest crossflow and lowest sweep angle, an approximate equilibrium turbulence scaling is not observed in the top-wall profile. Finally, figures 12(g) and 12(h) show the profiles at location x_r, where the flow reattaches, measured from the bottom and top walls, respectively. The profiles for Case B collapse with the ZPG profile. The profiles of cases C and D slightly deviate from the law of the wall. Near the reattachment zone, the flow is expected to be far from equilibrium, owing to the presence of large-scale coherent structures (Kiya & Sasaki 1985) and impingement of vortical structures on the wall (Shih & Ho 1994; Simpson 1996; Na & Moin 1998; Kaltenbach 2003; Dejoan & Leschziner 2004; Hudy, Naguib & Humphreys 2007), but only minor deviations with respect to the ZPG profile are observed. It appears that anisotropy introduced by the shear layer impingement is reduced by the strong turbulence maintained in the axial direction. Finally, the top wall profile for Case B follows the log law while slightly lower velocities are observed in the log-layer for cases C and D, which is indicative of an APG.

The mean pressure gradient along the net flow direction, as defined by the shear-stress coordinate system, is given by

$$\frac{\partial\langle p\rangle}{\partial s} = \nabla\langle p\rangle \cdot \boldsymbol{s}, \tag{5.1}$$

where $\langle p\rangle$ is the mean pressure and $\boldsymbol{s}$ is the net mean flow direction, i.e. in the θ direction. The profiles of $\partial\langle p\rangle/\partial s$, normalized by $1/2(\rho W_b^2/h)$, are shown in figure 13 along the crossflow direction on the bottom and top walls. The pressure gradient on the bottom wall attains a constant negative value away from the wire owing to the imposed FPG (negative $\partial\langle p\rangle/\partial s$) in all cases. Near the wire in the crossflow cases, three regions of large FPG are observed, which indicate the primary and two secondary separated-flow regions. The magnitude of FPG increases as the amount of crossflow is increased. Towards the reattachment point, the pressure gradient shows a linear increase, before it attains a constant negative value. Favourable pressure gradients are also observed on the top wall in all cases except Case D. Moreover, one region of large FPG is observed above the wire; note that the region is split in the middle by the periodic boundary used in the simulation. A linear increase of the pressure gradient is observed in the region above the primary separation bubble upstream of the reattachment point, followed by a decrease of the pressure gradient and a region with constant pressure gradient towards the centre of the channel. In Case D, a region of APG is observed for x/h approximately between 2 and 5. The profiles on the bottom and top wall indicate that equilibrium of the flow is reached towards the centre of the channel where the flow remains attached. This fast recovery process can be attributed to the presence of the strong axial flow.

The profiles of $\partial\langle p\rangle/\partial s$, normalized by $1/2(\rho W_b^2/h)$, on the wire surface are shown in figure 14. In Case A, the pressure gradient remains uniform on the wire surface. In the crossflow cases, on the windward surface of the wire, FPG is observed as the flow accelerates to overcome the area reduction caused by the wire. The magnitude of FPG increases as the amount of crossflow is increased. The pressure gradient reverses just before reaching the top-most point of the wire. Obviously, the flow can not sustain that APG for long and it separates quickly generating a shear layer, which

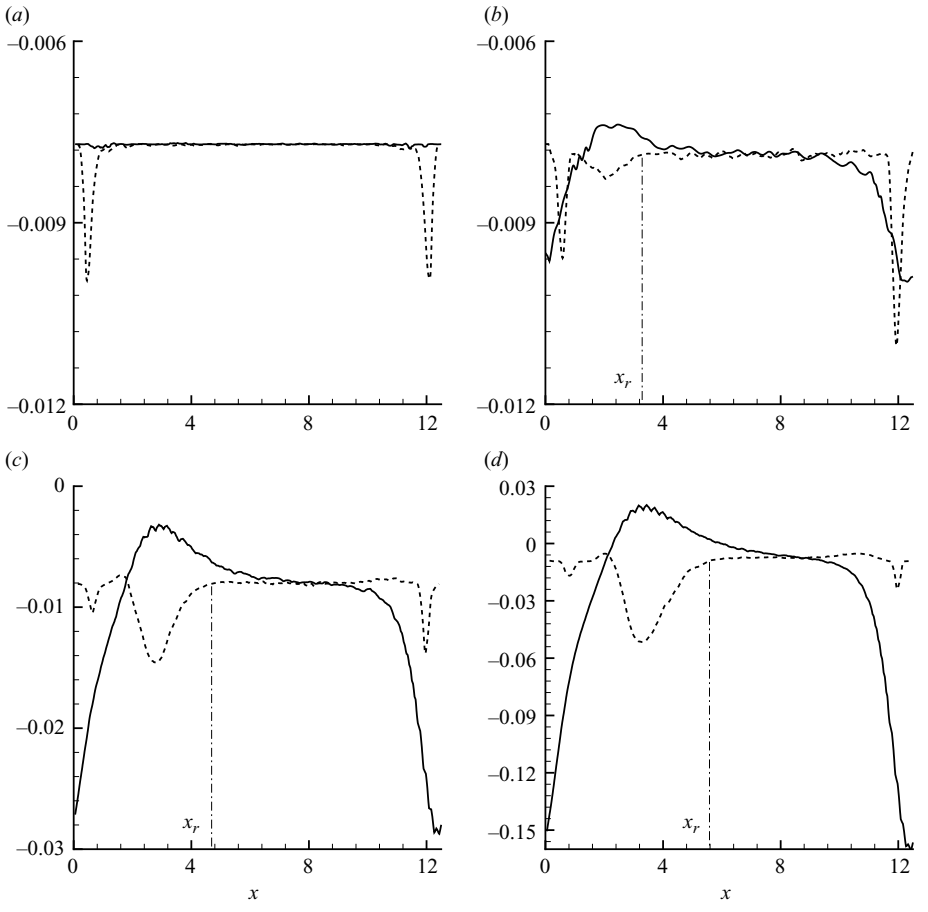

FIGURE 13. Pressure gradient $\partial\langle p\rangle/\partial s$, normalized by $1/2(\rho W_b^2/h)$, along the crossflow direction for cases A (a), B (b), C (c) and D (d) on bottom and top walls. Dashed line denotes profile on the bottom wall and solid line denotes profile on the top wall. Dashed-dotted line indicates the mean reattachment location.

can be seen qualitatively by the sudden drop of the pressure gradient at $\beta \approx 85°$. After separation, the pressure gradient takes small negative value on the leeward side of the wire. These results complement and are necessary in order to rationalize the observed behaviour of the inner-scaled velocity profiles discussed previously.

5.2. *Turbulence intensities*

Contours of turbulence kinetic energy, $k = (1/2)\langle u_i' u_i'\rangle$, normalized by W_b^2, in the x–y plane are shown in figure 15. In Case A, the peak of k is about 0.017 and it is observed close to the walls and wire surface and it reaches a minimum value towards the centre of the channel. The zone around the contact point of the wire with the walls of the channel does not experience the same level of turbulence kinetic energy as that observed in the less-confined regions of the flow. The proximity of the walls blocks the development of velocity fluctuations in that region. In Case B, the peak of k is about 0.019 and it is observed close to the walls, wire surface and shear layer. In the primary recirculation zone, k attains a value of about 0.005. After the flow reattaches, the contours are similar to those of Case A, with lower values observed

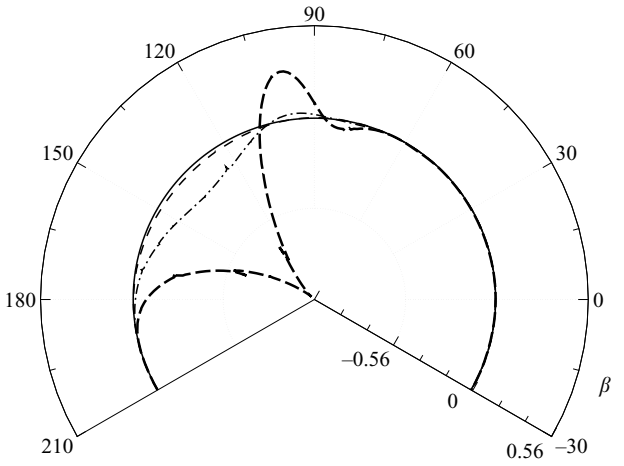

FIGURE 14. Pressure gradient $\partial\langle p\rangle/\partial s$, normalized by $1/2(\rho W_b^2/h)$, on the wire surface. Cases A, B, C and D are denoted by thin solid, thin dashed, thin dashed-dotted and thick dashed curves, respectively.

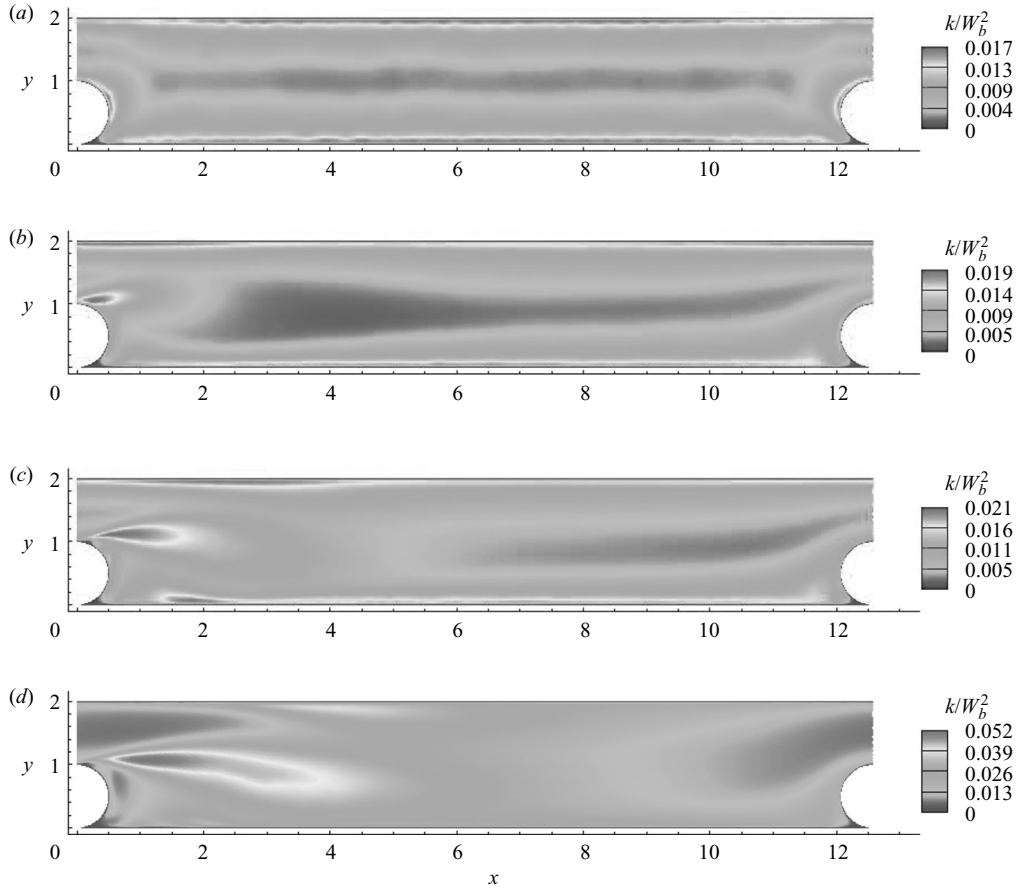

FIGURE 15. Turbulence kinetic energy normalized by W_b^2 for cases A (*a*), B (*b*), C (*c*) and D (*d*).

towards the middle of the channel. In Case C, peak k is about 0.021 and it is observed close to the wall within the recirculation bubble. The turbulence kinetic energy attains higher values near the region of separation and recirculation in comparison to other parts of the channel but there are two lower peaks of k, one at the shear layer and another close to the top wall of the channel in the neighbourhood of the wire. For Case D, the peak of k, approximately 0.052, is located in the shear layer. The regions of large k have grown in extent and magnitude compared to Case C. Lower values of k are observed in other parts of the channel. Part of the increase in kinetic energy is directly associated with the presence of the additional crossflow. This additional flow increases the overall Reynolds number, (3.17), and one would expect higher levels of kinetic energy as a direct consequence of the increase in the flowrate. Nevertheless, the interaction of crossflow with the axial flow result in additional turbulence production at specific locations.

One difficulty that must be considered when analysing the overall behaviour of statistical profiles as a function of y across the channel height is the impossibility of defining a unique flow direction valid over the extent of the channel. According to our previous parameterization, § 3.2, it is possible to define at least three different directions at any particular value of x. These are the two directions determined from the local mean wall shear stress, similar to (3.11), as well as a direction defined by the local average flowrate through this plane. The latter being analogous to the angle defined from Q_x and Q_z, appropriately rescaled. One immediately realizes that none of these angles provides a clear and unique direction at a particular station because the flow is not homogeneous in the x direction. Therefore, we chose to discuss the turbulence intensities in the frame of the simulation and avoid rotating the velocity components in any particular direction to prevent introducing an additional degree of arbitrariness.

The profiles of turbulence intensities, i.e. the root mean square (r.m.s.) velocity fluctuation, normalized by friction velocity at different crossflow locations, x_t, x_c, x_b and x_r, are shown in figures 16–19, respectively. The quantities u_{rms}, v_{rms} and w_{rms} denote crossflow, vertical and streamwise intensity, respectively. In Case A, the turbulence intensities attain higher values in the near-wall regions and lower values towards the centre of the channel. In the cases with crossflow, except in Case D, the largest change is observed in the values of w_{rms}, which attains a maximum value close to the top wall of the channel. The location of this maximum is about $y/h = 1.96$ in Case B and C. The relative values of the intensities change as the crossflow increases owing to the change in the mean direction of the flow. The value of w_{rms} in Case A is slightly lower in the near-wall region and slightly higher in the outer part of the boundary layer, in comparison to those of a flat plate boundary layer. This is consistent with the study of Snarski & Lueptow (1995) of a turbulent boundary layer on a cylindrical surface, where the difference in the turbulence intensity in the streamwise direction from a turbulent boundary layer on a flat surface was attributed to low surface area near the wall and less constraints in the outer region of the flow. Due to low surface area near the wire, less vorticity per unit volume is introduced in the boundary layer compared with a flat plate turbulent boundary layer. In the outer part of boundary layer the wire surface imposes fewer constraints on the flow and motion of the eddies, resulting in larger w_{rms} values compared to a flat plate turbulent boundary layer.

The profiles at x_c for Case A are approximately symmetric about the centre of the channel (the small asymmetry is due to limited statistical sampling) and they are similar to those of a turbulent channel (Kim, Moin & Moser 1987). This is due

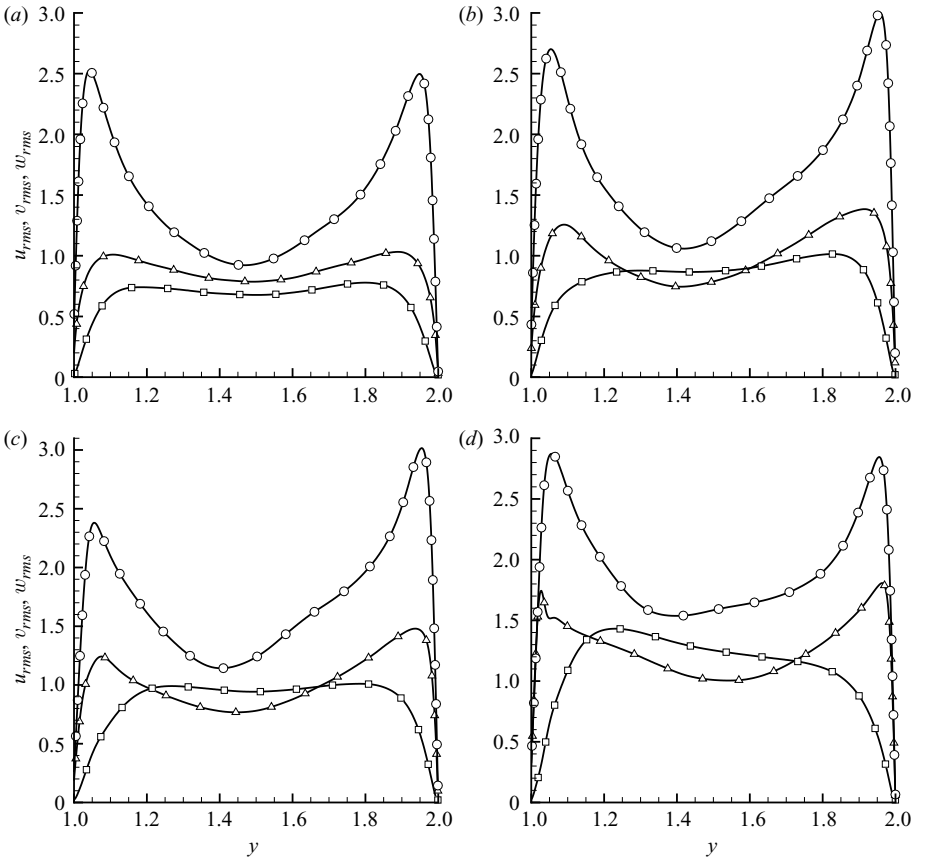

FIGURE 16. Root mean square (r.m.s.) velocity fluctuations normalized by friction velocity at location x_t. The different intensities are u_{rms} (Δ), v_{rms} ($\square$) and w_{rms} ($\circ$). Subfigures denote cases A (a), B (b), C (c) and D (d).

to the lack of separation of the flow in Case A and the effect of the wire is not significant towards the central region of the channel. In Case B, the profiles start to lose symmetry, indicating recovery of the flow in this region is not yet complete. The u_{rms} values are larger than the v_{rms} values in most of the channel except near the centre. In cases C and D, where the amount of crossflow is higher, the profiles loose their symmetry completely and the minimum value does not occur at the centre of the channel. The location of minimum turbulence intensity in Case C is observed towards the lower half of the channel. In this case, away from the wall, the u_{rms} and v_{rms} profiles do not vary significantly. In Case D, the value of u_{rms} increases away from the wire in the vertical direction and it attains higher values than those of w_{rms}. This increase can be attributed to a high turbulence kinetic energy in the outer part of the boundary layer (Johnston 1970) or a strong APG.

At location x_b, all profiles develop a peak in all r.m.s. of velocity components towards the centre of the channel. This is a consequence of the presence of the shear layer. The value of u_{rms} and v_{rms} increase in the near-wall and recirculation regions as the amount of crossflow increases. In the shear-layer region, both u_{rms} and v_{rms} become comparable to w_{rms} implying a higher level of turbulence intensities. This is similar to the high turbulence intensity observed in shear layers in earlier studies of

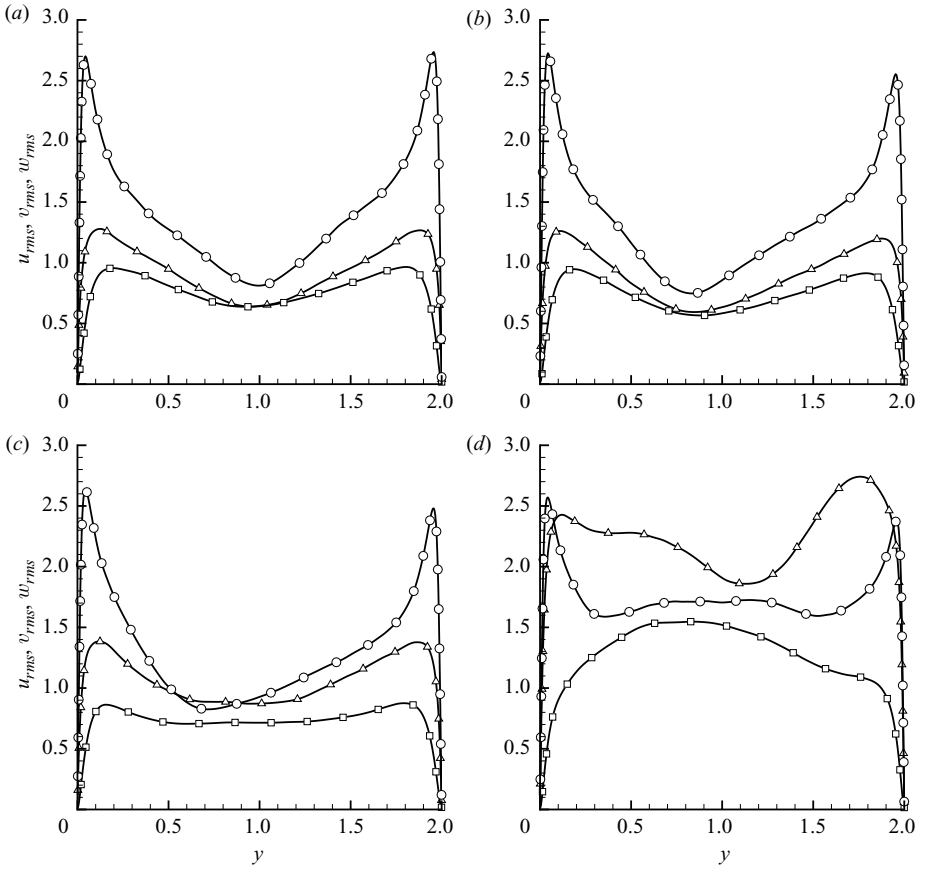

FIGURE 17. Root mean square velocity fluctuations normalized by friction velocity at location x_c. The different intensities are u_{rms} (Δ), v_{rms} ($\square$) and w_{rms} ($\circ$). Subfigures denote cases A (a), B (b), C (c) and D (d).

separating/reattaching flows (Eaton & Johnston 1981; Shih & Ho 1994; Liua *et al.* 2008). Kaltenbach & Janke (2000) have attributed such an increase of turbulence intensity in the shear layer of a swept flow, to the extensional strain of vortical structures along their axis, present in the shear layer. In swept flows, the vortices, which are not aligned with the flow direction, experience this strain owing to presence of large velocity gradient components in the shear layer.

Finally, the profiles at x_r, where the mean flow reattaches to the wall, are similar to those of a turbulent channel for cases B and C, with peak values near the wall and the presence of a local minimum towards the centre. However, in Case D the profile shows substantial differences. The maximum value of u_{rms} increases as the amount of crossflow increases. The value of v_{rms} is highest near the walls and shows less variation towards the centre of the channel, increasing with increasing crossflow. This region shows that decay of turbulence intensity starts to occur near the reattachment region. This decay is more apparent in cases B and C, compared to Case D.

6. Resolution requirements for a corresponding large-eddy simulation

Almost without exception, flows in industrial or technological applications at high Reynolds numbers cannot be studied using DNS. The high Reynolds numbers and

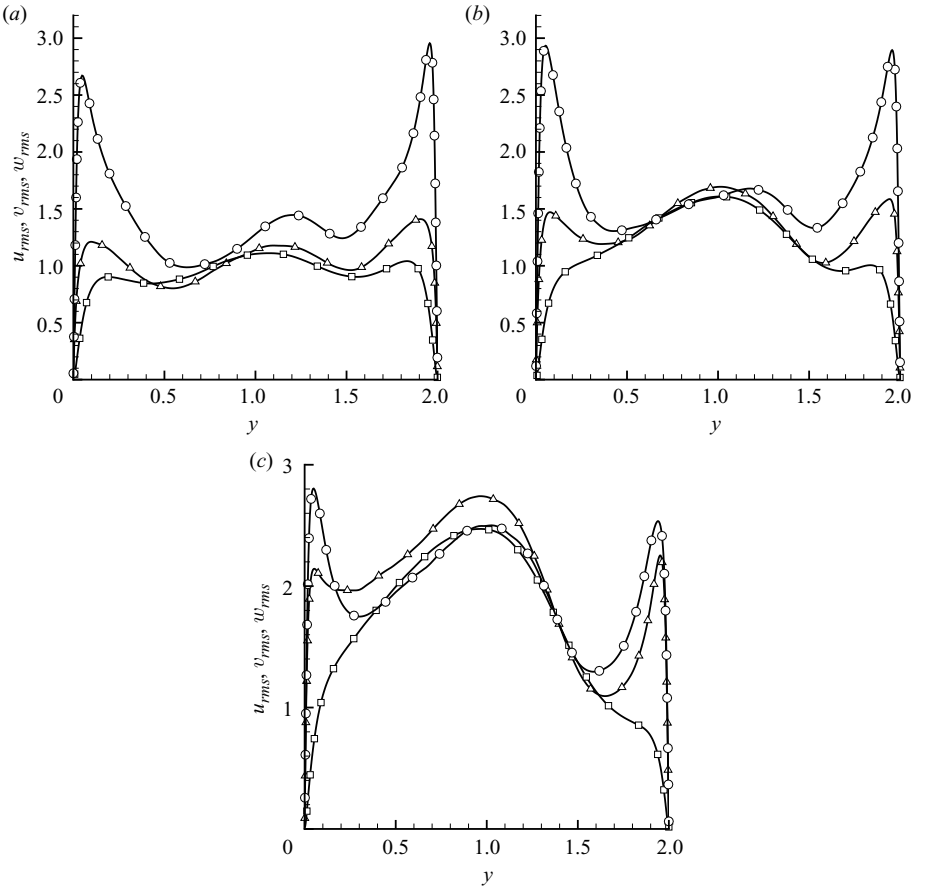

FIGURE 18. Root mean square velocity fluctuations normalized by friction velocity at location x_b. The different intensities are u_{rms} (Δ), v_{rms} ($\square$) and w_{rms} ($\circ$). Subfigures denote cases B (*a*), C (*b*) and D (*c*).

complex geometries of these flows make the computational cost prohibitive. Therefore, one is forced to consider some degree of turbulence modelling, e.g. LES. One difficulty that is often encountered in this approach is that it is rarely possible to assess *a priori* the accuracy of the simulation due to subgrid and numerical modelling uncertainties (Pope 2004; Geurts 2006; Meyers, Sagaut & Geurts 2006). In this respect, the present DNS datasets can provide a potential candidate for a LES validation. Unfortunately, for complex flows, it is often unknown how to select the cutoff scale of the LES such that an accurate representation of the flow is achieved, i.e. without carrying out a costly refinement study (Meyers, Geurts & Baelmans 2003). Here, we discuss an *a posteriori* estimate of the required cutoff scale of a LES corresponding to each of the present DNS cases, such that all features of interest are appropriately captured. In order to achieve this, we utilize the often implied (heuristic) criteria that states that a good LES is one that resolves most of the energy containing scales (Pope 2004). In our particular application, the ultimate goal would be to estimate the actual resolution requirements of a full LES of the complete wire-wrapped assembly of a reactor core; involving hundred of pins with helically wrapped wires.

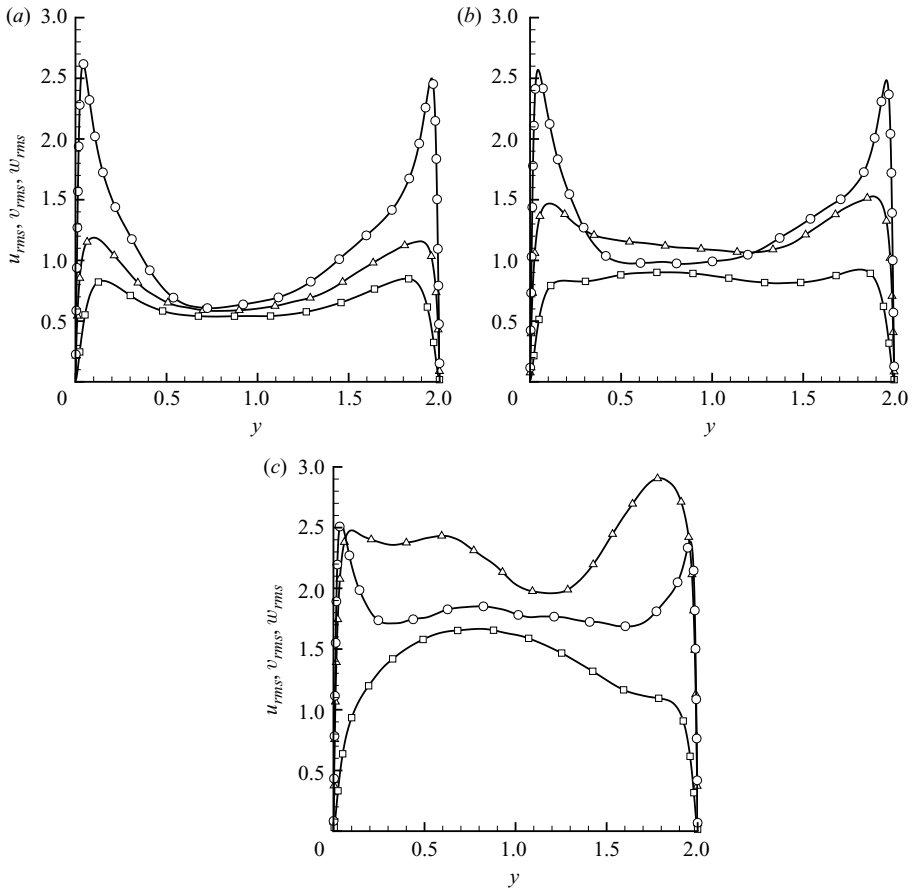

FIGURE 19. Root mean square velocity fluctuations normalized by friction velocity at location x_r. The different intensities are u_{rms} (Δ), v_{rms} ($\square$) and w_{rms} ($\circ$). Subfigures denote cases B (a), C (b) and D (c).

Following Pope (2000), let us consider the integral length scale L expressed in terms of turbulence kinetic energy k and turbulence dissipation ϵ given by

$$L = \frac{k^{3/2}}{\epsilon}. \tag{6.1}$$

The turbulence Reynolds number Re_L based on the integral length scale is given by

$$Re_L = \frac{k^2}{\epsilon \nu}. \tag{6.2}$$

The profiles of Re_L at four different crossflow locations for cases A through D are shown in figure 20. The value of Re_L is larger in Case D compared to other cases at all the crossflow locations which is consistent with a larger value of Re_b in Case D. Different criteria can be utilized to determine the fraction of turbulence kinetic energy that should be resolved in a LES such that unavoidable modelling uncertainties do not pollute the overall simulation accuracy; one such criteria is discussed in Pope (2004). According to that view, a 'good' LES should resolve at least 80 % of the turbulence kinetic energy at any location of the domain. This requires a mesh resolution fine

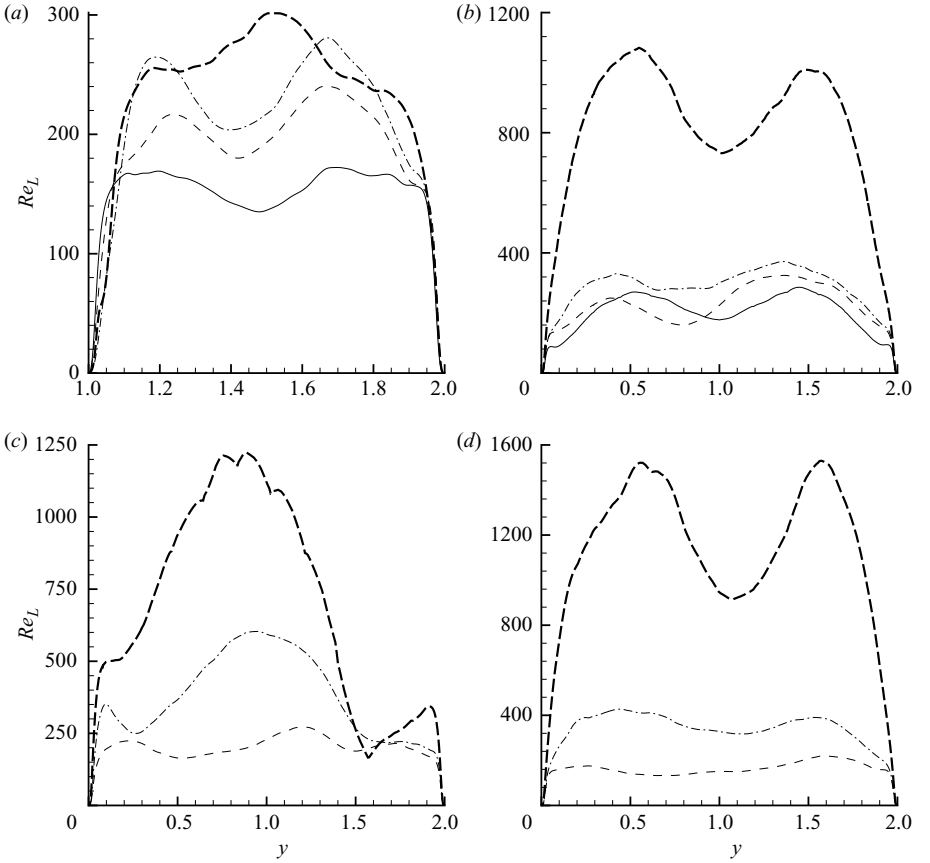

FIGURE 20. Profiles of integral Reynolds number, Re_L for cases A through D at four different crossflow locations: x_t (*a*), x_c (*b*), x_b (*c*) and x_r (*d*). Cases A, B, C and D are denoted by thin solid, thin dashed, thin dashed-dotted and thick dashed curves, respectively.

enough to capture the energy associated with most of the large-scale eddies. In the case of a separating/reattaching flow, it is important to know whether the resolution required near the reattachment and recirculation zones is higher or lower than that required in other regions of the flow, where an understanding of the resolution needs is well established.

In order to answer this question for the present flows, some assumptions must be invoked. In particular, an estimate of the energy spectra is required at all locations of the flow. Given the limited statistical sample available from the DNS, we propose to use a model spectrum to derive the resolution estimates of interest here. The model spectrum of Pope (2000) can be used to obtain a non-dimensional cutoff wavenumber κ_c such that the range from $\kappa = 0$ to κ_c contains 80 % of the total turbulence kinetic energy. The turbulence kinetic energy is related to the energy spectra (assuming isotropy and homogeneity but not necessarily an inertial subrange scaling) by

$$k = \int_0^\infty E(\kappa)\,\mathrm{d}\kappa, \tag{6.3}$$

where $E(\kappa)$ denotes the energy spectrum. The cutoff wavenumber κ_c can be defined implicitly through the 80 % low-pass spectral filter given by

$$0.8\ k = \int_0^{\kappa_c} E(\kappa)\,\mathrm{d}\kappa. \tag{6.4}$$

The model spectrum proposed by Pope (2000) is

$$E(\kappa) = C\epsilon^{2/3}\kappa^{-5/3} f_L(\kappa L) f_\eta(\kappa\eta), \tag{6.5}$$

where f_L and f_η are non-dimensional functions given by

$$f_L(\kappa L) = \left(\frac{\kappa L}{[(\kappa L)^2 + c_L]^{1/2}}\right)^{5/3+p0} \tag{6.6}$$

and

$$f_\eta(\kappa\eta) = \exp\{-\beta\{[(\kappa\eta)^4 + c_\eta^4]^{1/4} - c_\eta\}\}, \tag{6.7}$$

respectively. The values of the constants we use are $p_0 = 2$, $\beta = 5.2$ and $C = 1.5$. After some manipulations, one can reduce the relationships to the group $\zeta = \kappa_c L$; a function of Re_L only. The constants c_L and c_η, at a fixed Re_L, can be found by solving (6.3) together with the turbulence dissipation relationship,

$$\epsilon = 2\nu \int_0^\infty \kappa^2 E(\kappa)\,\mathrm{d}\kappa. \tag{6.8}$$

The group $\zeta = \kappa_c L$ can be used to define the physical cutoff scale, according to

$$\frac{\Delta_c}{h} = \frac{\pi}{\zeta}\frac{L}{h}. \tag{6.9}$$

Note that the present estimates are not tied to a particular discretization or subgrid-scale model (e.g. Meyers, Geurts & Sagaut 2007). They reflect the lowest order criteria for appropriate LES of the flows discussed in this paper if all uncertainties are surrogate to the subgrid modelling error. The profiles of Δ_c/h at four different crossflow locations are shown in figure 21 for cases A through D. In particular, it appears that one can resolve the flow in the LES sense using at least $\Delta_c/h \sim 0.05$ at all locations (this corresponds to a mesh of $250 \times 40 \times 500 = 5\ 10^6$ grid points with an overall savings of a factor of 20 with respect to the present DNS). Figure 22 shows the same results but using inner scaled variables. In this case the estimate predicts that an inner-scaled cutoff scale of $\sim$20 should be sufficient to resolve the flow close to the wall in a LES.

7. Shear stress analysis

The statistics of the shear stress on the bottom wall and the wire surface are investigated at this point. The magnitude of the wall shear stress is given by

$$\tau_s = \sqrt{\tau_{ln}^2 + \tau_{mn}^2}, \tag{7.1}$$

where τ_{ln} and τ_{mn} are the wall-shear stresses, as defined in (3.9) and (3.10). In the present discussion, a completely local investigation is carried out where the wall shear stresses are not projected along the average shear-stress direction, defined by the angle θ in (3.11). This was done to focus on the local character of the flow, as opposed to investigating quantities that combine elements determined from averages and which

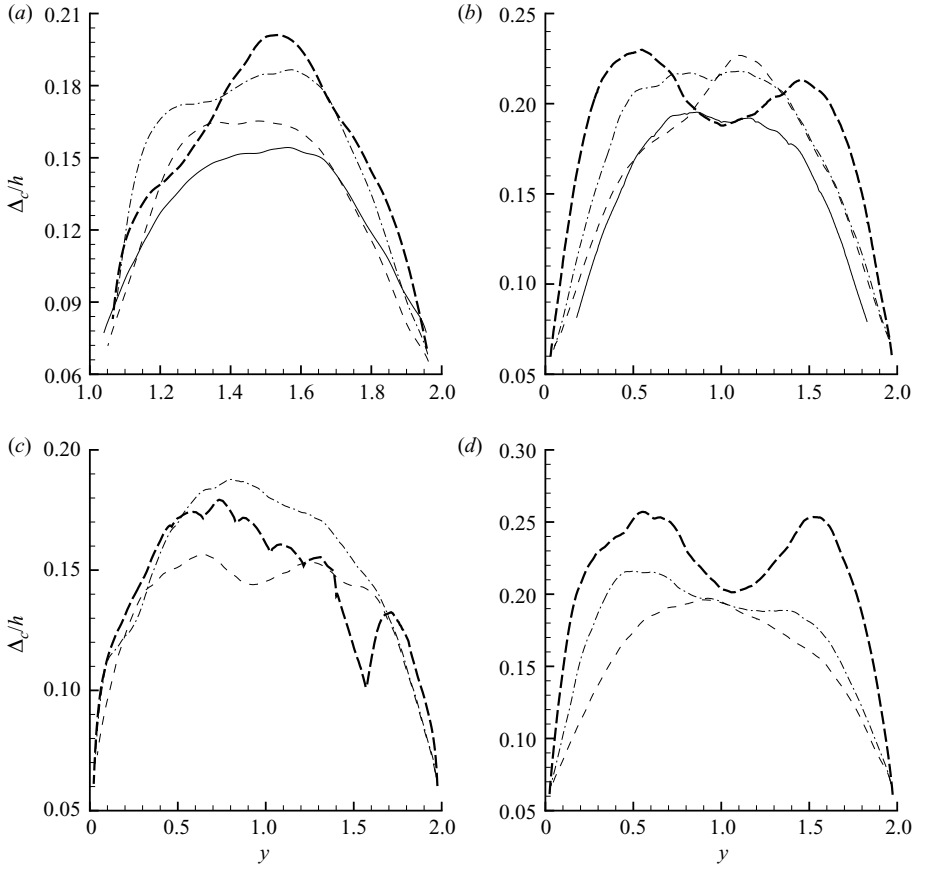

FIGURE 21. Profiles of Δ_c/h for cases A through D at four different crossflow locations: x_t (*a*), x_c (*b*), x_b (*c*) and x_r (*d*). Cases A, B, C and D are denoted by thin solid, thin dashed, thin dashed-dotted and thick dashed curves, respectively.

could potentially skew the interpretation of the small-scale physical process involved. Irrespective of this choice, (7.1) is invariant with respect to the use of a local or an average θ.

Iso-contours of total shear stress τ_s, normalized by τ_c, are shown in figures 23 and 24. In Case A, figure 23 shows intermittent streaks of high shear stress between low shear stress regions. The streaks are mostly aligned along the mean flow direction, as expected. The region close to the wire, which extends roughly up to 2 wire diameters, contains weaker structures but the qualitative pattern of the shear stress is analogous to that observed in the centre of the channel. However, the distribution looks different in Case C, where figure 24 shows distinct patterns or regions with varying shear-stress behaviour. In the region covering the reattachment zone to the centre of the channel, very high shear-stress values are observed. Here, intermittent high shear-stress streaks embedded in low shear-stress regions are observed. The streaks are aligned at an angle with the axial direction owing to the presence of the crossflow. In the recirculation region, the shear stress distribution shows less well-defined intermittent patterns. The reduced intensity of the streaky structures is similar to that observed in previous studies Spalart & Coleman 1997; Kaltenbach 2003; Marquillie, Laval & Dolganov 2008). A sharp change in the magnitude is

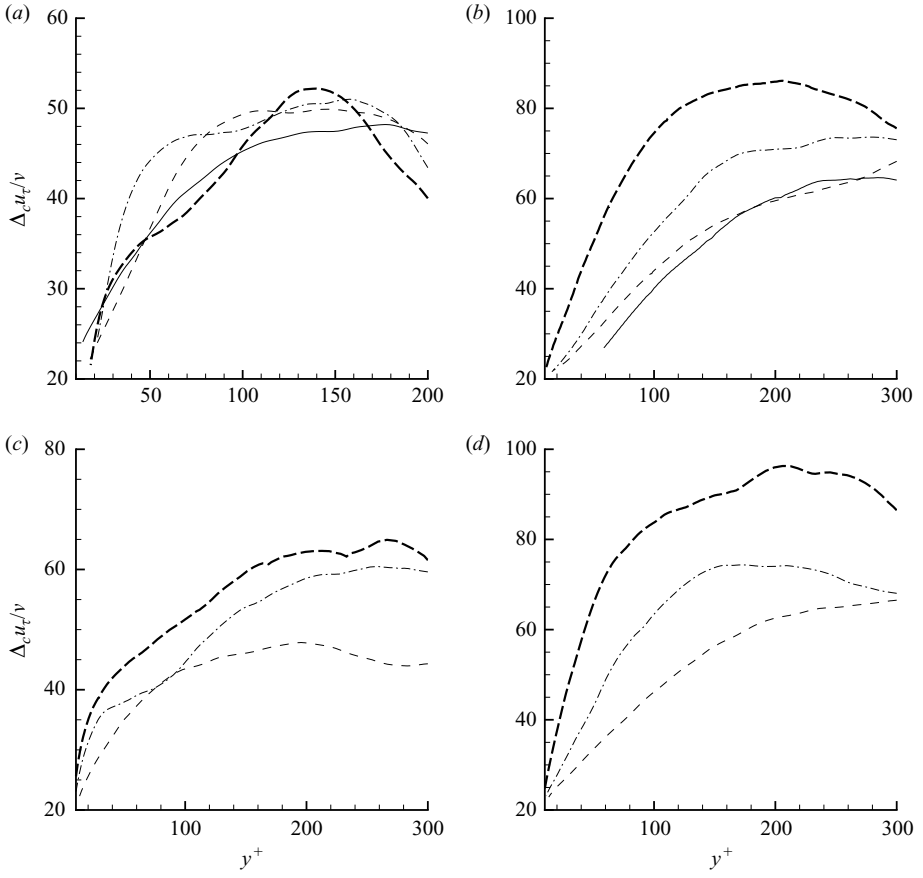

FIGURE 22. Profiles of $\Delta_c u_\tau/\nu$ for cases A through D at four different crossflow locations: x_t (a), x_c (b), x_b (c) and x_r (d). Cases A, B, C and D are denoted by thin solid, thin dashed, thin dashed-dotted and thick dashed curves, respectively.

also observed around the reattachment point. The intermittent or streaky behaviour observed towards the centre of the channel is similar to the streaky pattern of velocity near the wall observed in channel flow and turbulent boundary layers (Simpson 1996; Kaltenbach 2003). The wall shear stress streaks in both cases seem to align with the mean flow direction. This alignment indicates convection of coherent structures in the net mean flow direction. The presence of these streaks indicates a high level of shear rate, which in turn is responsible for production of turbulence kinetic energy near the wall (Kim *et al.* 1987; Kaltenbach 2003). Honkan & Andreopoulos (1997) have also observed similar intermittent behaviour in several invariants associated with strain-rate and vorticity and have attributed this to a burst of large amplitude events followed by less violent periods. Near the reattachment, this streaky behaviour is reduced owing to the impinging of vortical structures on the wall but the shear stress remains high. The effect of impinging structures is not felt downstream of the reattachment zone as axial flow dominates in that region.

An overlay plot of vortical structures and wall shear stress is shown in figure 25. The instantaneous wall shear stress distribution appears to be well correlated with the shape and orientation of vortical structures. As discussed earlier, in the regions where the flow is attached, the wall shear stress shows intermittent behaviour with high shear

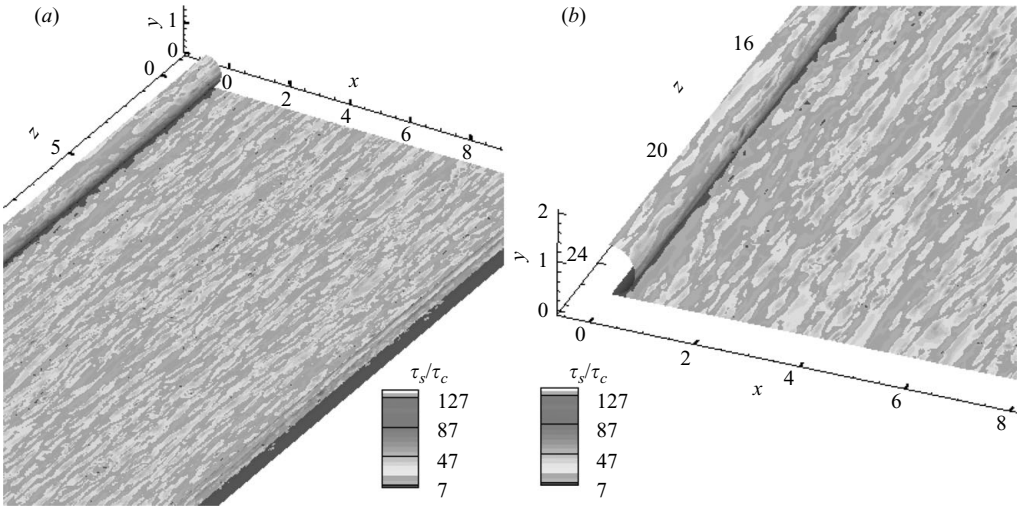

FIGURE 23. Iso-contours of friction stress τ_s, normalized by τ_c, on the bottom wall including the wire surface for Case A. Large-scale view of the wall shear stress (a), and a zoom in of the near-wire region (b).

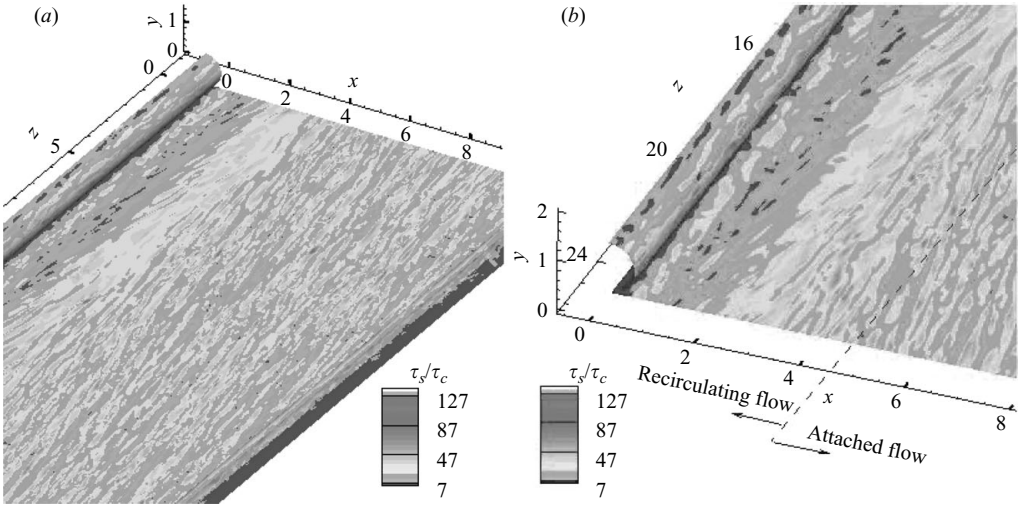

FIGURE 24. Iso-contours of friction stress τ_s, normalized by τ_c, on the bottom wall including the wire surface for Case C. Large-scale view of the wall shear stress (a) and shows a zoom in of the near-wire region (b).

stress regions embedded within low shear stress regions. However, the region under the recirculation bubble is characterized by a low and almost constant wall shear stress. Note that on the wire top, where the flow is partially attached, quasi-streamwise structures like v_1 are observed. In the regions where the flow detaches and forms a shear layer, structures like v_2 are observed with no specific orientation. However close to the wall in the recirculation zone, some slender streamwise structures similar to v_3 are observed. After the flow reattaches, quasi-streamwise slender vortices like v_4 are again evident.

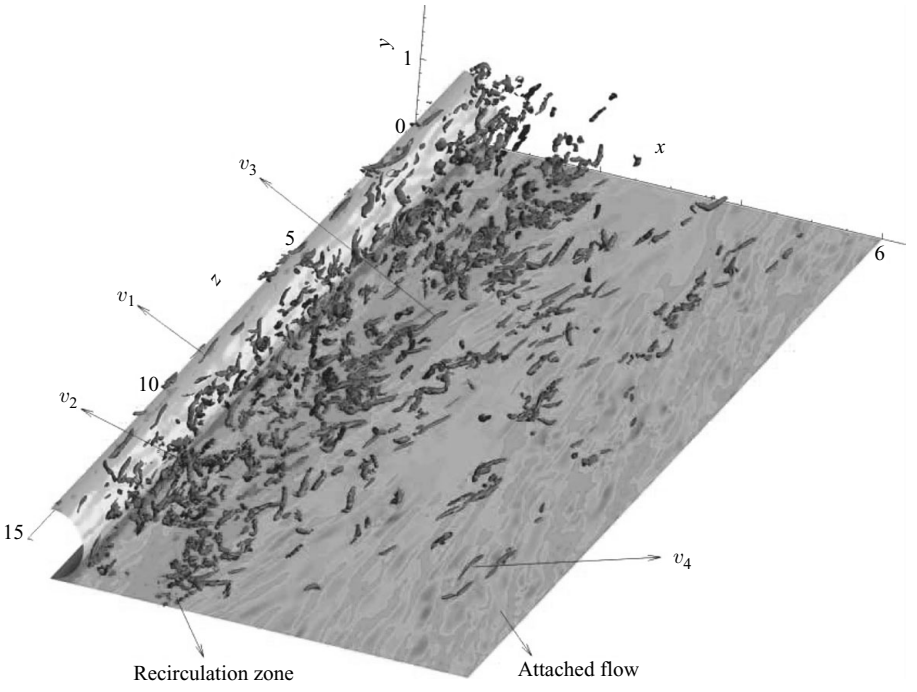

FIGURE 25. Wall shear stress overlayed with vortical structures in the near-wall region for Case C identified by $W_b^2\lambda_2/h^2 = -4.06$. Representative vortical structures are indicated by v_1, v_2, v_3 and v_4.

7.1. *Mean and root mean square wall shear stress*

The variation of τ_w, defined in (3.20) and normalized by τ_c, as a function of x along the bottom wall is shown in figure 26 for all the cases. In Case A, τ_w remains fairly constant approximately two diameters away from the wire and decreases gradually as one approaches the wire. As discussed in § 5.1, a reduction in the axial velocity gradient is observed close to the wire which in turn leads to a reduction in τ_w in this region. In the cases with crossflow, the maximum value of τ_w increases with increasing crossflow. The location of maximum wall shear stress is observed to occur near reattachment. Away from the wire, where the crossflow is attached, τ_w remains fairly constant. This constant value increases with the amount of crossflow since the resultant mean flowrate increases from cases B to D. In the leeward side of the wire, it shows a gradual increase with increasing x, reaching a maximum near the mean crossflow reattachment point. This gradual increase is observed in all the cases with crossflow, although it is very small in Case B. The lower values of τ_w observed inside the primary and secondary recirculation bubble in the leeward side and secondary recirculation bubble in the windward side, compare qualitatively with observations of Dianat & Castro (1991) and Mittal *et al.* (2003). This behaviour is consistent with the earlier studies of separating/reattaching flows mentioned in § 1, where wall shear stress variation in the streamwise direction has been used to determine the reattachment length. However, in the present case, the criteria of zero wall shear stress at the reattachment location cannot be used to determine a reattachment length (Johnston 1970). The zero crossing of the wall shear stress is a particular condition encountered in unswept flows.

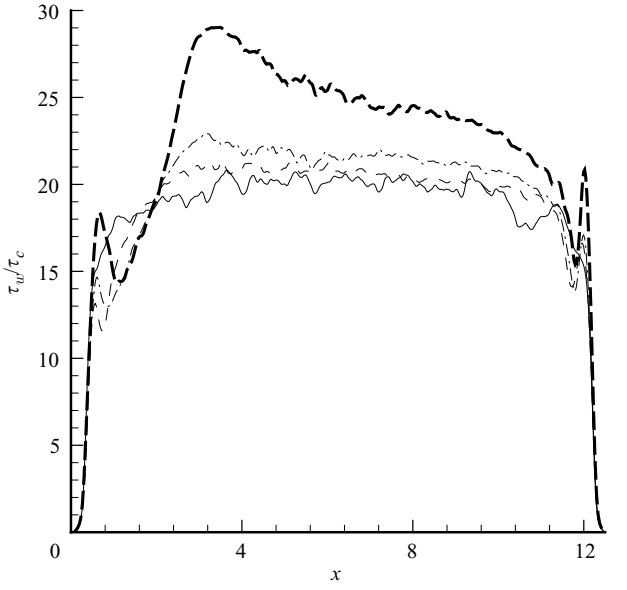

FIGURE 26. Variation of mean wall shear stress τ_w normalized by τ_c along crossflow direction on the bottom wall. Cases A, B, C and D are denoted by thin solid, thin dashed, thin dashed-dotted and thick dashed curves, respectively.

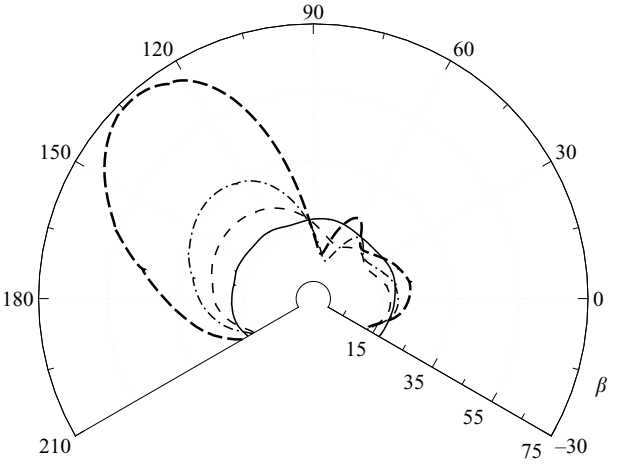

FIGURE 27. Variation of mean wall shear stress τ_w normalized by τ_c on the wire surface. Cases A, B, C and D are denoted by thin solid, thin dashed, thin dashed-dotted and thick dashed curves, respectively.

The variation of the mean wall shear stress on the wire surface is shown in figure 27 in polar coordinates. The variation for Case A is nearly symmetric, as expected, except close to the contact point of the wire. In the cases with crossflow, symmetry is not observed as crossflow is accelerating in the windward side and decelerating in leeward side of the wire. In particular, the value of τ_w is higher in the windward side owing to the flow acceleration and increased wall friction. Overall, the wall shear stress increases with increasing crossflow. Similar profiles are observed in channel flow with a constriction (Mittal *et al.* 2003).

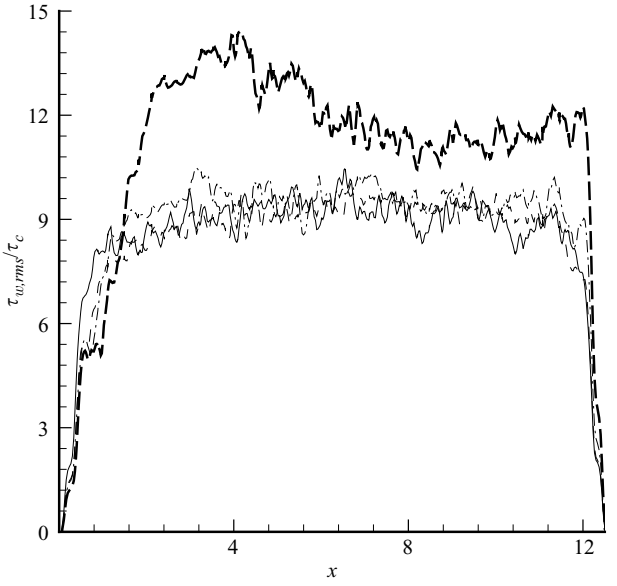

FIGURE 28. Variation of $\tau_{w,rms}$ normalized by τ_c along crossflow direction on the bottom wall. Cases A, B, C and D are denoted by thin solid, thin dashed, thin dashed-dotted and thick dashed curves, respectively.

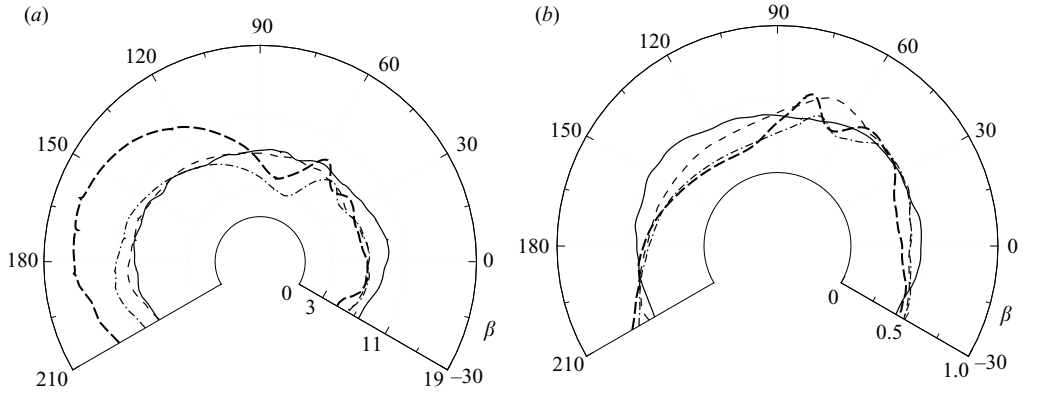

FIGURE 29. Variation of r.m.s. of mean wall shear stress, $\tau_{w,rms}$, normalized by τ_c (a) and τ_w (b) on the wire surface. Cases A, B, C and D are denoted by thin solid, thin dashed, thin dashed-dotted and thick dashed curves, respectively.

The r.m.s. of wall shear stress $\tau_{w,rms}$, normalized by τ_c, is shown in figure 28 as a function of x along the bottom wall for all cases. The behaviour of the mean and r.m.s. of τ_w are very similar. Larger r.m.s. values, about 50 % of the mean, are observed in Case D near the reattachment. This is similar to the observations near reattachment in the earlier studies of separating/reattaching flow (Dianat & Castro 1991; Kaltenbach & Janke 2000; Mittal *et al.* 2003; Li & Naguib 2005). This rise is attributed to impingement of large-scale vortical structures in the reattachment region. After reattachment of the flow, a gradual decay and levelling off is observed.

The variation of the r.m.s. of wall shear stress normalized by τ_c and τ_w, respectively, on the wire surface is shown in figure 29 in polar coordinates. Nearly symmetric

behaviour is observed for Case A, although some variation is observed which is attributed to slightly lower convergence of these second-order statistics. In the cases with crossflow, the symmetric behaviour is lost. When scaled by τ_c, the r.m.s. of wall shear stress attains larger values on the windward side of the wire, which is apparent in cases C and D. This is similar to the behaviour observed in unswept flows, where the higher levels of wall shear stress fluctuations are associated closely with acceleration of the mean flow (Nepomuceno & Lueptow 1997). Note that the r.m.s. of wall shear stress shown in figure 29(*a*) is scaled by τ_c, which is based on the bulk velocity in the axial direction, and thus it does not take into account the crossflow. An alternative scaling is based on the local value of the average wall shear stress. When this scaling is used, as shown in figure 29(*b*), $\tau_{w,rms}/\tau_w$ decreases with increasing crossflow, which can be attributed to the dampening effect of FPG.

7.2. *Wall shear stress alignment*

The net mean flow direction is based on a wall shear stress coordinate system, discussed by Simpson (1996). The orientation of the wall shear stress with respect to the mean flow is important from a modelling point of view. Appropriate modelling of the near-wall region, including anisotropic effects, is believed to be very important for improved simulations based on RANS as well as in LES. Linear eddy-viscosity models assume that the strain rate tensor is aligned with the turbulent shear stresses, but previous studies show that it is the wall shear stresses that are aligned with the turbulent shear stresses close to the wall (Johnston 1970; Bradshaw 1987; Webster *et al.* 1996). In this section, the behaviour of θ, defined by (3.11), is investigated. This definition implies that θ is a mean angle computed from quantities that were averaged in the homogeneous z direction. The variation of this angle as a function of x on the bottom wall is shown in figure 30 for all the cases. The angle is very small in Case A because there is no crossflow; the shear stress vector is mostly aligned along the axial direction. For the cases with crossflow, negative values of angle θ are observed in the leeward side of the wire. This is a consequence of the mean crossflow reversal within the recirculation zone. The absolute value of θ increases with increasing crossflow. After flow reattachment, the angle becomes positive and increases with increasing x to reach a constant value until the secondary recirculation bubble in the windward side of the wire is reached. Within this last region, the angle changes sign for the same reason explained before for the primary recirculation zone. The variation observed in θ is consistent with the mean wall shear stress variation shown in figure 26. Moreover, θ could be used to define the reattachment length, as the point where θ becomes zero, and it could be viewed as a generalization of the zero wall-shear stress condition used in unswept flows. Another feature of θ is that it is indicative of the degree of flow recovery after reattachment.

The average wall shear stress alignment θ can be used as a criterion to quantify the degree and rate at which the flow attains equilibrium after reattachment. Figure 30 shows, for cases B through D, the mean reattachment location x_r as well as the approximate location where the flow appears to reach equilibrium x_e. Figure 30 shows that after reattachment θ increases in the region $x_r < x < x_e$, reaching a constant level some distance ahead of the secondary recirculation bubble on the windward side of the wire. The length of this recovery region increases with increasing crossflow velocity. For cases C and D, equilibrium turbulent flow is not recovered before the influence of the wire is beginning to be felt again. Especially for Case D, the simulation domain length in the x direction is not sufficient for the flow to recover completely. The length of the recovery region varies since the Reynolds number in the crossflow direction

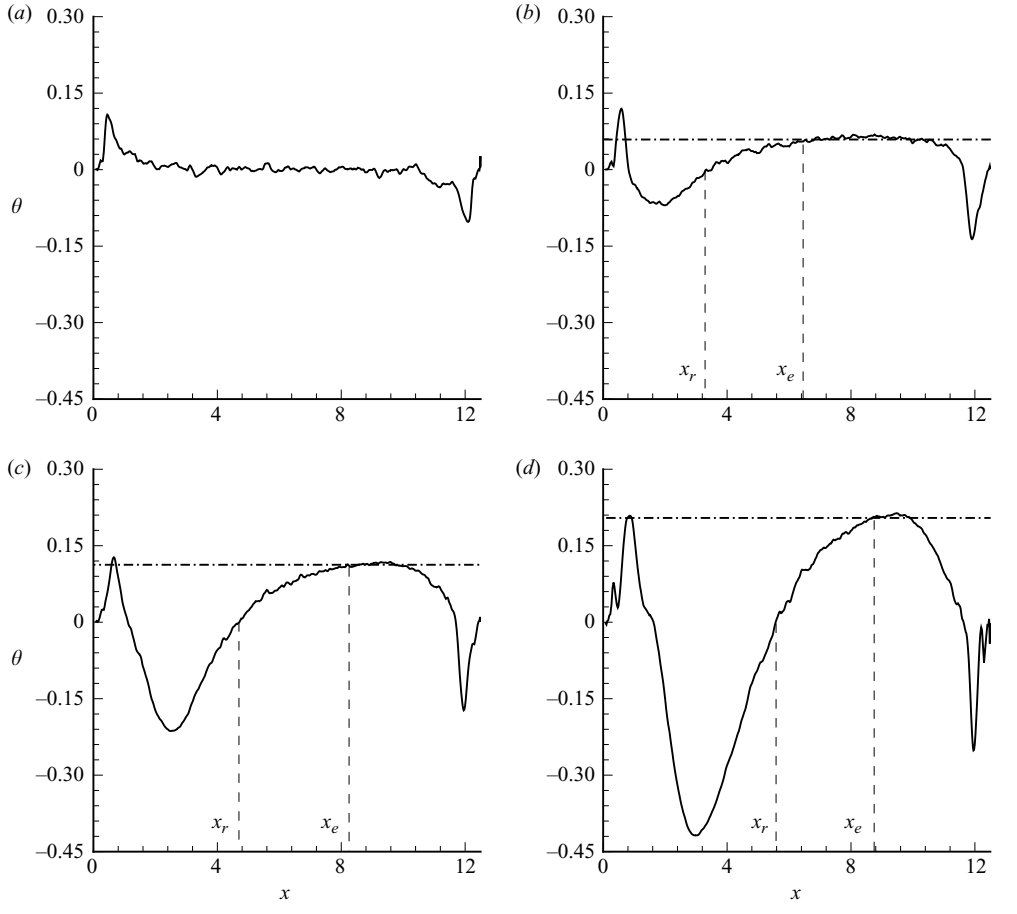

FIGURE 30. Variation of angle θ (in *radians*) along crossflow direction for all the cases: Case A (*a*), Case B (*b*), Case C (*c*) and Case D (*d*). The equilibrium level of angle θ is denoted by the dashed-dotted line.

is increasing from cases B to D. Therefore, a combined effect of sweep angle and Re affects the recovery length. This observation is also consistent with the pressure gradient behaviour in the mean flow direction, as shown in figure 13.

The variation of θ on the wire surface is shown in figure 31. In these plots, the corner regions of the wire are excluded because appropriate convergence of the mean shear stresses could not be realized; θ exhibited too large fluctuations in that region. In all cases with crossflow, an increase of θ with increasing crossflow velocity is observed on the windward side of the wire, with a maximum value in the region ($90^\circ < \beta < 180^\circ$). Moreover, little variation is observed in the leeward side of the wire. Here, the wall shear stress, $\langle \tau_{mn} \rangle$, is quite small. The variation of θ on the wire surface is consistent with the mean wall shear stress variation shown in figure 27.

8. Conclusions

Results of DNS of turbulent swept flow over a wire resting on a wall of a channel are presented. Axial and crossflow Reynolds numbers are 5400 and 0–1709, respectively. Spectral element method/Fourier decomposition is used to solve the governing

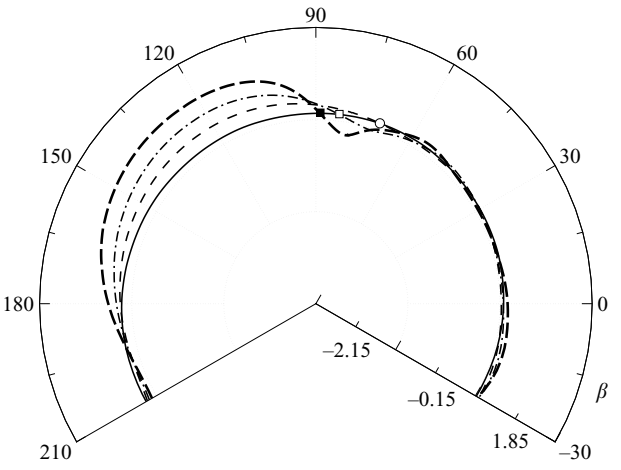

FIGURE 31. Variation of θ (in *radians*) on the wire surface. Cases A, B, C and D are denoted by thin solid, thin dashed, thin dashed-dotted and thick dashed curves, respectively. Symbols (○), (□) and (■) denote the separation location for cases B, C and D, respectively.

equations. The present study is concerned with crossflow velocities up to 32 % of the axial velocity. This regime has received little attention in the past. Increasing crossflow magnitudes and Reynolds numbers for a fixed axial flowrate increases the size of the recirculation region on the leeward side of the wire. Instantaneous vortical flow structures show clear contrast in the separated and attached regions in terms of their orientation with respect to the mean flow direction. Mean velocity profiles, Reynolds stresses and turbulence kinetic energy are investigated and their behaviour in the recirculation bubbles is discussed. As in many other wall-bounded turbulent flows with detached flow regions, the inner-scaled mean velocity profile in the shear-stress-based coordinate frame shows large deviations from 'Law of the Wall' behaviour. Some of these deviations can clearly be associated with variations in the pressure gradient, showing flow recovery to a near equilibrium state after reattachment.

The instantaneous total wall shear stress shows intermittent streaks of high value embedded in low shear stress regions in the case without crossflow. These streaks are aligned in the net mean flow direction. In the cases with crossflow, away from the reattachment zone, the streaky nature of the shear stress is observed with the streaks aligning along the net mean flow direction. Near the reattachment zone and under the primary recirculation bubble the intermittent streaky character is not as marked owing to the impingement of vortical structures from the shear layer. The instantaneous wall shear distribution appears to be well correlated with the shape and orientation of vortical structures, with larger values close to the reattachment zone. The angle between components of wall shear stress vector, θ, is negative in the leeward side of the wire. It increases in the crossflow direction and reaches a peak and remains constant further downstream until the windward side of the wire is reached. The statistics of the angle θ indicates that the attached flow approaches equilibrium but only at a rather low pace.

Finally, the DNS is used to evaluate the extent of the resolution requirements in a hypothetical LES. This is estimated according to the 80 % kinetic energy resolution criteria and it is shown that LES of the present flows should be possible using at most a factor of 20 fewer grid points (using a subgrid scale model). In particular, this

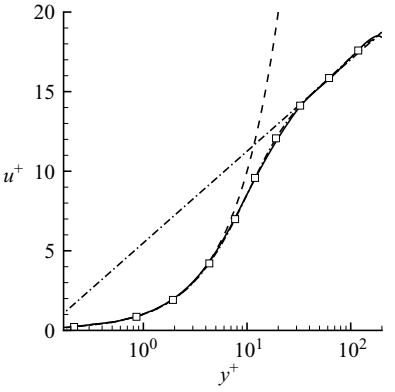

FIGURE 32. Profile of mean streamwise velocity normalized by wall-shear velocity, compared with the 'Law of the Wall' and DNS data of Kim *et al.* (1987). Solid line is simulation data, dashed line is $u^+ = y^+$ and dashed-dotted line is $u^+ = 2.5\ \ln y^+ + 5.5$. Symbol □ denotes DNS data of Kim *et al.* (1987).

can be used to obtain an estimate of the required resolution of a simulation of the full wire-wrapped assembly in a nuclear reactor.

This work was supported in part by Argonne National Laboratory under subcontract 7F-01201 and by the centre for the Simulation of Advanced Rockets supported by the U.S. Department of Energy through the University of California under subcontract B523819. This research used resources of the Argonne Leadership Computing Facility at Argonne National Laboratory, which is supported by the Office of Science of the U.S. Department of Energy under contract DE-AC02-06CH11357.

Appendix A. Validation

The code was validated against the reference DNS of Kim *et al.* (1987). This corresponds to the simulation of a turbulent channel flow at Reynolds number of 3300, based on the centreline velocity, and friction Reynolds number of 180. The simulation is performed using the same numerical procedure detailed in § 3.1, with a total of approximately 4 million grid points collocated as in Kim *et al.* (1987). The mean velocity profile obtained from the validation simulation, the reference DNS, is compared with the reference 'Law of the Wall' is shown in figure 32. The turbulence intensity profiles compared with results from the reference DNS are shown in figure 33. Excellent and good agreement is observed in the mean velocity and turbulence intensity profiles, respectively.

Appendix B. Turbulence kinetic energy budgets

The budget equation for the turbulence kinetic energy k is given by

$$\underbrace{\frac{\partial}{\partial t}k + \langle u_j\rangle\frac{\partial}{\partial x_j}k}_{\text{Convection}} = \underbrace{-\langle u_i'u_j'\rangle\frac{\partial\langle u_i\rangle}{\partial x_j}}_{\text{Production}} \underbrace{-\nu\left\langle\frac{\partial u_i'}{\partial x_j}\frac{\partial u_i'}{\partial x_j}\right\rangle}_{\text{Dissipation}}$$
$$\underbrace{-\frac{1}{2}\frac{\partial}{\partial x_j}\langle u_i'u_i'u_j'\rangle}_{\text{Turbulent transport}} + \underbrace{\nu\frac{\partial^2}{\partial x_j\partial x_j}k}_{\text{Viscous diffusion}} \underbrace{-\frac{1}{\rho}\frac{\partial}{\partial x_i}\langle u_i'p'\rangle}_{\text{Pressure transport}}, \quad \text{(B 1)}$$

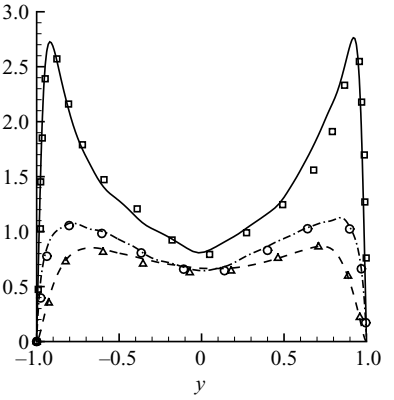

FIGURE 33. Profile of turbulence intensities compared with DNS results of Kim *et al.* (1987). Symbols □, Δ and ○ denote DNS data of Kim *et al.* (1987) whereas lines denotes validation simulation data for u_{rms}, v_{rms} and w_{rms}, respectively. Solid line is u_{rms}, dashed line is v_{rms} and dashed-dotted line is w_{rms}.

where, P, T, ϵ, π, $\mathscr{D}$ and $\mathscr{C}$ denotes turbulence production, transport, dissipation, pressure transport, viscous diffusion and convection, respectively. The profiles of the terms P, T, ϵ, π, $\mathscr{D}$ and $\mathscr{C}$ throughout the span of the channel are obtained at location x_c for Case A and at location x_b for the remaining cases. These profiles are shown in figure 34. The location x_b is important as it covers the shear-layer region. In Case A, the peaks of all the budget terms are located near the top and bottom walls. Towards the centre of the channel, all the budget terms become insignificant because in this region the turbulence kinetic energy is small. In the cases with crossflow, peaks are also observed near both walls and towards the centre of the channel, where the shear layer is located. The value of the local peaks of these quantities increases with increasing crossflow. This increase is clearly observed in cases C and D in the shear-layer region. As the amount of crossflow increases, the transport terms, T and π along with dissipation, balances the production of turbulence kinetic energy in the recirculating region. The production term P, becomes dominant in the region of the separated shear layer and the magnitude increases with the amount of crossflow. This is consistent with a rise in the level of turbulence intensity in this region in all the three directions, as discussed earlier. In the shear-layer region, an increase is observed in the magnitude of all the budget terms as the amount of crossflow increases signifying transport of turbulent energy across the shear layer. Above the shear-layer zone, it is observed that the turbulent transport in conjunction with the convection term becomes a source of turbulence kinetic energy. Near the wall, dissipation is balanced by viscous diffusion (Na & Moin 1998).

Appendix C. Statistics of the recirculation bubble

The type of reattachment observed in the present simulations is of ordinary type according to Johnston (1970). In this case, the wall shear stress is not zero at the reattachment point. The observed reattachment length in the simulations increases with increasing Re; similar to findings over backward-facing steps (Armaly *et al.* 1983; Adams & Johnston 1988; Li & Naguib 2005). The shear layer that separates the recirculation bubble from the main channel is characterized by the presence of disorganized vortical structures (Chun & Sung 2003; Song & Eaton 2004). The

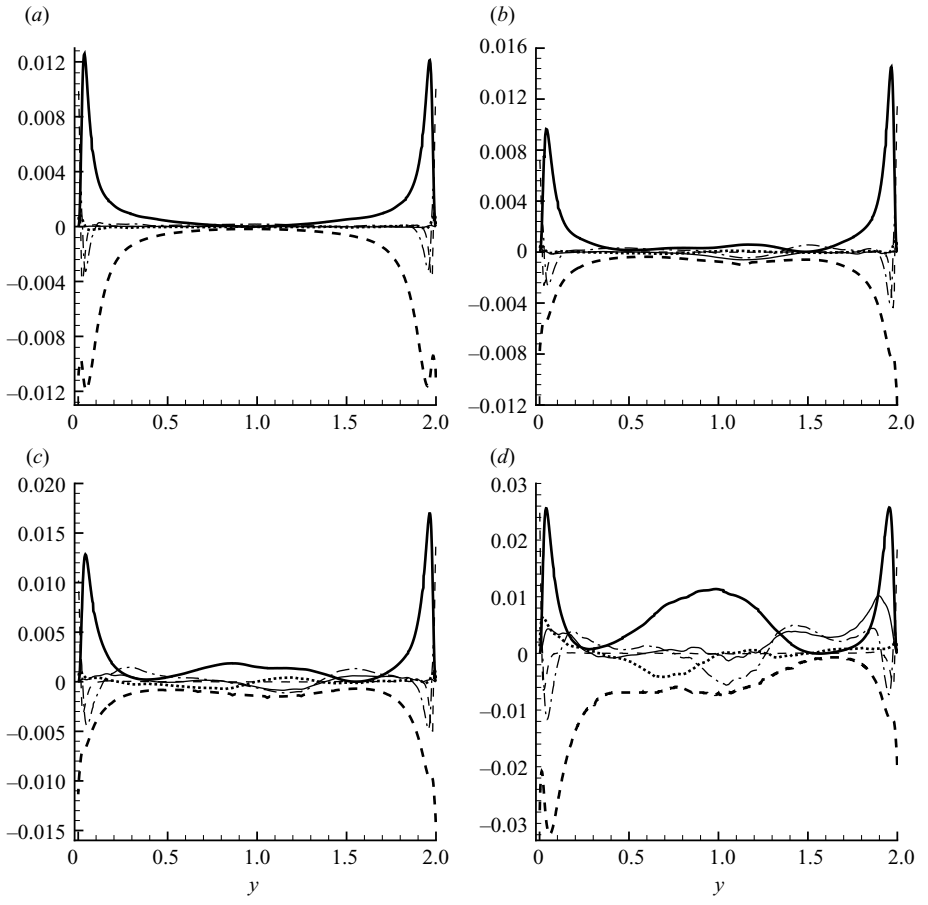

FIGURE 34. Profiles of turbulence kinetic energy budget terms at location x_c for Case A (a) and at location x_b for cases B (b), C (c) and D (d). P, T, π, $\mathscr{D}$, $\mathscr{C}$ and ϵ are denoted by thick solid line, dashed-dotted line, dotted line, dashed line, solid line and thick dashed line, respectively.

intensity of the turbulence kinetic energy is large, as discussed earlier. The locus of the peak of k in the shear layer along with the mean dividing streamline and iso-contours of k normalized by W_b^2, for Case C are shown in figure 35. The locus of peak turbulence kinetic energy is usually used as an approximation for the centre of the shear layer (Dianat & Castro 1991). At the separation point, this curve deviates from the mean dividing streamline but it remains close to the mean dividing streamline over most of the primary recirculation zone. Further deviation of the peak turbulence kinetic energy locus and the mean dividing streamline is observed before reattachment. This would suggest that the outer regions near reattachment still contains high values of turbulent intensity and there is persistence of large scale vortical structures; similar to that observed in backward-facing step flow (Eaton & Johnston 1981). Some studies of the behaviour of this shear layer have focused on the fluid entrainment (Li & Naguib 2005; Liu *et al.* 2006, 2007) and its association with the reattachment length.

An important difference between the present flows and previous studies is that a large fraction of the primary bubble is in a fully turbulent state; caused by the large axial flow. Iso-contours of turbulent production P, normalized by W_b^3/h, are

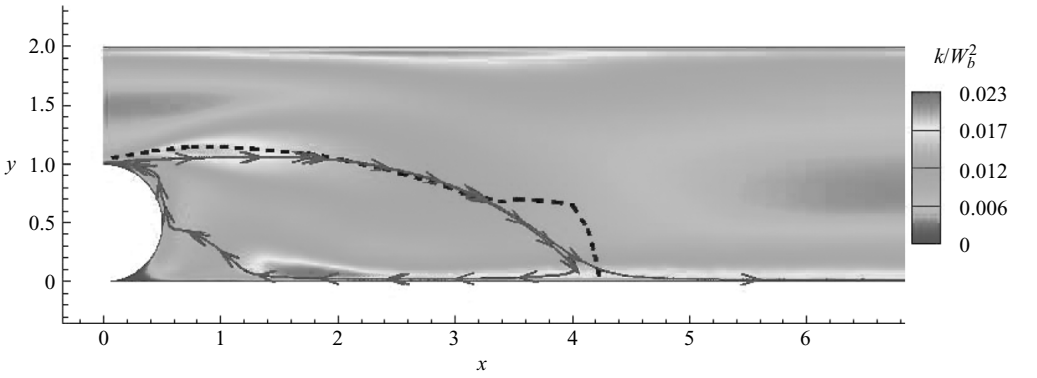

FIGURE 35. Iso-contours of turbulence kinetic energy normalized by W_b^2, overlayed with mean streamlines (solid curves with arrows) and locus of maximum kinetic energy (dotted curve) in the shear layer for Case C.

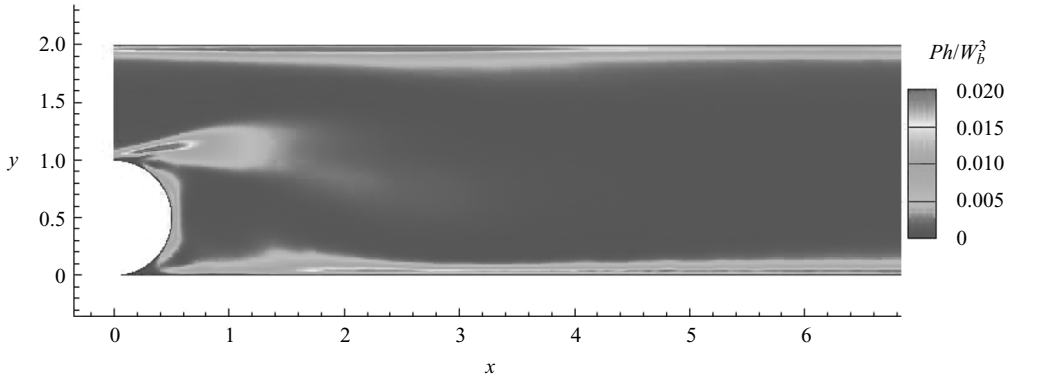

FIGURE 36. Iso-contours of production of turbulence kinetic energy normalized by W_b^3/h for Case C.

shown in figure 36 for Case C. It is observed that production is high close to the separation point and beginning of the shear layer as well as close to the wall within the recirculation zone. The level of near-wall turbulence production in the recirculation and fully attached flow regions is similar. This indicates that the flow within the recirculation bubble has features of a turbulent flow compared to other separated/reattached flows where the flow within the recirculation bubble has more laminar features (Dianat & Castro 1991). The magnitude of the turbulence kinetic energy and production decreased in the shear layer away from separation. This implies a rapid decay of the vortical structures before impingement on the wall. The turbulence kinetic energy and production have much smaller values under the secondary smaller recirculation bubble close to the wire. Figure 15 shows that the turbulence kinetic energy is large just before the secondary separation. This flow resembles, to some extent, separation induced in a flat turbulent boundary layer by an imposed adverse pressure gradient. A decrease in FPG can be seen in figure 13(a) at approximately $x = 1.5$, which is close to the location of the flow separation observed in figures 35 and 36.

Finally, the turbulence energy spectra for Case C at four locations are shown in figure 37. A reference line corresponding to $-5/3$ power-law is also shown in the plots

Location	x/h	y/h	y^+
Shear layer	2.17	1.04	324
Centre of bubble	2.01	0.58	181
Near reattachment	3.61	0.17	53
Centre of channel	6.31	1.00	312

TABLE 4. Coordinates of the locations where turbulence energy spectra is obtained.

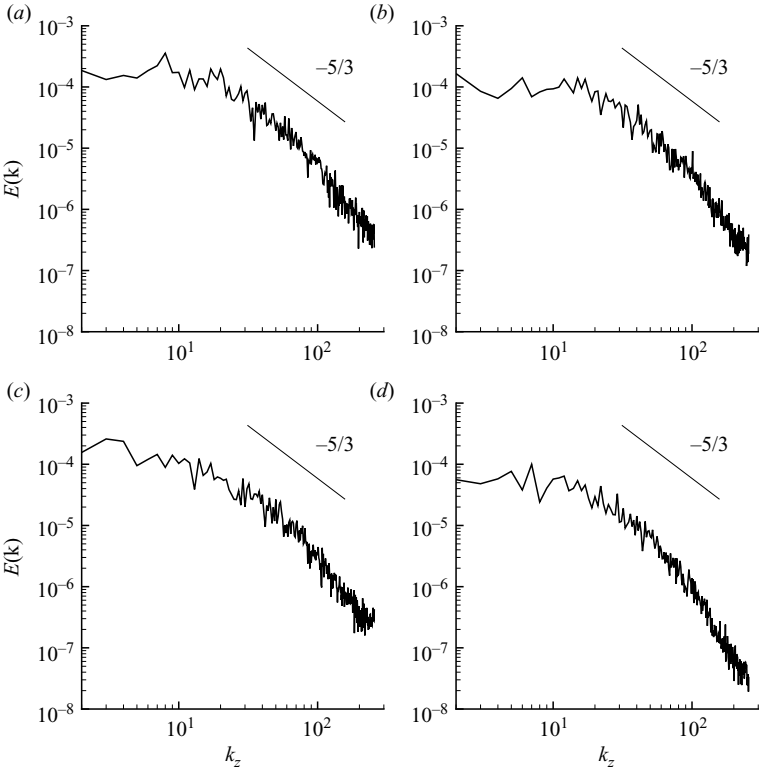

FIGURE 37. Energy spectra for Case C at four different crossflow locations, shear layer (*a*), centre of recirculating bubble (*b*), near reattachment location (*c*) and centre of channel (*d*).

to compare with inertial subrange Kolmogorov scaling. Spectra are shown for points located in the centre of the shear layer, in the centre of the bubble, near reattachment location inside the bubble and at the centre of the channel. The x, y and y^+ coordinates of these locations are provided in table 4. The inner coordinate y^+ is measured from the bottom wall. It is observed that in the intermediate wavenumber range, the energy decay may approximate the $-5/3$ power-law, although the Reynolds number is not sufficiently large for an inertial subrange to be clearly defined. Nevertheless, the level of turbulence kinetic energy and the shape of the spectra clearly indicates that the flow is fully turbulent within a large fraction of the primary recirculation bubble.

REFERENCES

ACHARYA, S., DUTTA, S., MYRUM, T. A. & BAKER, R. S. 1994 Turbulent flow past a surface-mounted two-dimensional rib. *J. Fluids Engng* **116**, 238–246.

Adams, E. W. & Johnston, J. P. 1988 Effects of the separating shear layer on the reattachment flow structure. Part 2. Reattachment length and wall shear stress. *Exp. Fluids* **6**, 493–499.

Angele, K. P. & Muhammad-Klingmann, B. 2006 PIV measurements in a weakly separating and reattaching turbulent boundary layer. *Eur. J. Mech.* – B/*Fluids* **25** (2), 204–222.

Armaly, B. F., Durst, F., Pereira, J. C. F. & Schönung, B. 1983 Experimental and theoretical investigation of backward-facing step flow. *J. Fluid Mech.* **127**, 473–496.

Bradshaw, P. 1987 Turbulent secondary flows. *Annu. Rev. Fluid Mech.* **19**, 53–74.

Bradshaw, P. & Wong, F. 1972 The reattachment and relaxation of a turbulent shear layer. *J. Fluid Mech.* **52**, 113–135.

Camussi, R., Felli, M., Pereira, F., Aloisio, G. & Marco, A. D. 2008 Statistical properties of wall pressure fluctuations over a forward-facing step. *Phys. Fluids* **20**, 075113.

Caruelle, B. & Ducros, F. 2003 Detached-eddy simulations of attached and detached boundary layers. *Intl J. Comput. Fluid Dyn.* **17**, 433–451(19).

Chun, S. & Sung, H. J. 2003 Large-scale vortical structure of turbulent separation bubble affected by unsteady wake. *Exp. Fluids* **34**, 572–584.

Deck, S. & Thorigny, P. 2007 Unsteadiness of an axisymmetric separating-reattaching flow: numerical investigation. *Phys. Fluids* **19**, 065103.

Dejoan, A. & Leschziner, M. A. 2004 Large eddy simulation of periodically perturbed separated flow over a backward-facing step. *Intl J. Heat Fluid Flow* **25** (4), 581–592.

Dianat, M. & Castro, I. P. 1991 Turbulence in a separated boundary layer. *J. Fluid Mech.* **226**, 91–123.

Eaton, J. K. & Johnston, J. P. 1981 A review of research on subsonic turbulent flow reattachment. *AIAA J.* **19**, 1093–1100.

Farabee, T. M. & Casarella, M. J. 1986 Measurements of fluctuating wall pressure for separated/reattached boundary layer flows. *J. Vib. Acoust. Stress. Reliab. Des.* **108**, 301–307.

Fröhlich, J., Mellen, C. P., Rodi, W., Temmerman, L. & Leschziner, M. A. 2005 Highly resolved large-eddy simulation of separated flow in a channel with streamwise periodic constrictions. *J. Fluid Mech.* **526**, 19–66.

Gallaire, F., Marquillie, M. & Ehrenstein, U. 2007 Three-dimensional transverse instabilities in detached boundary layers. *J. Fluid Mech.* **571**, 221–233.

Geurts, B. 2006 Interacting errors in large-eddy simulation: a review of recent developments. *J. Turbul.* **7** (55) 1–16.

Griffith, M. D., Thompson, M. C., Leweke, T., Hourigan, K. & Anderson, W. P. 2007 Wake behaviour and instability of flow through a partially blocked channel. *J. Fluid Mech.* **582**, 319–340.

Henderson, R. D. 1994 Unstructured spectral element methods: parallel algorithms and simulations. PhD thesis, Princeton University, Princeton, NJ.

Henderson, R. D. & Karniadakis, G. E. 1995 Unstructured spectral element methods for simulation of turbulent flows. *J. Comput. Phys.* **122**, 191–217.

Honkan, A. & Andreopoulos, Y. 1997 Vorticity, strain-rate and dissipation characteristics in the near-wall region of turbulent boundary layers. *J. Fluid Mech.* **350**, 29–96.

Hudy, L. M., Naguib, A. & Humphreys, W. M. 2007 Stochastic estimation of a separated-flow field using wall-pressure-array measurements. *Phys. Fluids* **19**, 024103.

Hwang, R. R., Chow, Y. C. & Peng, Y. F. 1999 Numerical study of turbulent flow over two-dimensional surface mounted ribs in a channel. *Intl J. Numer. Methods Fluids* **31**, 767–785.

Jeong, J. & Hussain, F. 1995 On the identification of a vortex. *J. Fluid Mech.* **285**, 69–94.

Jeong, J., Hussain, F., Schoppa, W. & Kim, J. 1997 Coherent structures near the wall in a turbulent channel flow. *J. Fluid Mech.* **332**, 185–214.

Johnston, J. P. 1970 Measurements in a 3-dimensional turbulent boundary layer induced by a swept, forward facing step. *J. Fluid Mech.* **42**, 823–844.

Kaiktsis, L. & Monkewitz, P. A. 2003 Global destabilization of flow over a backward-facing step. *Phys. Fluids* **15**, 3647.

Kaltenbach, H.-J. 2003 The effect of sweep-angle variation on the turbulence structure in a separated, three-dimensional flow. *Theor. Comput. Fluid Dyn.* **16** (3), 187–210.

Kaltenbach, H.-J. & Janke, G. 2000 Direct numerical simulation of flow separation behind a swept, rearward-facing step at $Re_H = 3000$. *Phys. Fluids* **12**, 2320.

Karniadakis, G. E. 1999 Simulating turbulence in complex geometries. *Fluid Dyn. Res.* **24**, 343–362.

Karniadakis, G. E., Israeli, M. & Orszag, S. A. 1991 High-order splitting methods for the incompressible Navier–Stokes equations. *J. Comput. Phys.* **97**, 414–443.

Kays, W. M. & Crawford, M. E. 2004 *Convective Heat and Mass Transfer*. McGraw Hill.

Kiel, R. & Vieth, D. 1995 Experimental and theoretical investigations of the near-wall region in a turbulent separated and reattached flow. *Exp. Therm. Fluid Sci.* **11** (3), 243–254.

Kim, J., Moin, P. & Moser, R. 1987 Turbulence statistics in fully developed channel flow at low Reynolds number. *J. Fluid Mech.* **177**, 133–166.

Kiya, M. & Sasaki, K. 1985 Structure of large-scale vortices and unsteady reverse flow in the reattaching zone of a turbulent separation bubble. *J. Fluid Mech.* **154**, 463–491.

Laskowski, G. M. & Durbin, P. A. 2007 Direct numerical simulations of turbulent flow through a stationary and rotating infinite serpentine passage. *Phys. Fluids* **19**, 015101.

Le, H., Moin, P. & Kim, J. 1997 Direct numerical simulation of turbulent flow over a backward-facing step. *J. Fluid Mech.* **330**, 349–374.

Lee, I. & Sung, H. J. 2002 Multiple-arrayed pressure measurement for investigation of the unsteady flow structure of a reattaching shear layer. *J. Fluid Mech.* **463**, 377–402.

Li, Y. & Naguib, A. M. 2005 High-frequency oscillating-hot-wire sensor for near-wall diagnostics in separated flows. *AIAA J.* **43** (3), 520–529.

Liu, Y. Z., Ke, F., Chen, H. P. & Sung, H. J. 2006 A wall-bounded turbulent mixing layer flow over an open step. I. Time-mean and spectral characteristics. *J. Turbul.* **7** (65), 1–17.

Liu, Y. Z., Ke, F., Chen, H. P. & Sung, H. J. 2007 A wall-bounded turbulent mixing layer flow over an open step. Part 2. Unsteady characteristics. *J. Turbul.* **8** (26), 1–17.

Liua, Y. Z., Ke, F. & Sung, H. J. 2008 Unsteady separated and reattaching turbulent flow over a two-dimensional square rib. *J. Fluids Struct.* **24**, 366–381.

Marquillie, M. & Ehrenstein, U. 2003 On the onset of nonlinear oscillations in a separating boundary-layer flow. *J. Fluid Mech.* **490**, 169–188.

Marquillie, M., Laval, J.-P. & Dolganov, R. 2008 Direct numerical simulation of a separated channel flow with a smooth profile. *J. Turbul.* **9**, 1–23.

Mellen, C. P., Fröhlich, J. & Rodi, W. 2000 Large eddy simulation of the flow over periodic hills. In *Proc. IMACS World Congress* (ed. M. Deville & R. Owens), Lausanne, Switzerland.

Meyers, J., Geurts, B. & Baelmans, M. 2003 Database analysis of errors in large-eddy simulation. *Phys. Fluids* **15** (9), 2740–2755.

Meyers, J., Geurts, B. & Sagaut, P. 2007 A computational error-assessment of central finite-volume discretizations in large-eddy simulation using a Smagorinsky model. *J. Comput. Phys.* **227** (1), 156–173.

Meyers, J., Sagaut, P. & Geurts, B. 2006 Optimal model parameters for multi-objective large-eddy simulations. *Phys. Fluids* **18** (095103).

Mittal, R., Simmons, S. P. & Najjar, F. 2003 Numerical study of pulsatile flow in a constricted channel. *J. Fluid Mech.* **485**, 337–378.

Moin, P. & Mahesh, K. 1998 Direct numerical simulation: a tool in turbulence research. *Annu. Rev. Fluid Mech.* **30**, 539–578.

Muppidi, S. & Mahesh, K. 2007 Direct numerical simulation of round turbulent jets in crossflow. *J. Fluid Mech.* **574**, 59–84.

Na, Y. & Moin, P. 1998 Direct numerical simulation of a separated turbulent boundary layer. *J. Fluid Mech.* **374**, 379–405.

Nepomuceno, H. G. & Lueptow, R. M. 1997 Pressure and shear stress measurements at the wall in a turbulent boundary layer on a cylinder. *Phys. Fluids* **9**, 2732–2739.

Nickels, T. B. 2004 Inner scaling for wall-bounded flows subject to large pressure gradients. *J. Fluid Mech.* **521**, 217–239.

Peller, N. & Manhart, M. 2006 *New Results in Numerical and Experimental Fluid Mechanics V*. Springer.

Pope, S. B. 2000 *Turbulent Flows*. Cambridge University Press.

Pope, S. 2004 Ten questions concerning the large-eddy simulation of turbulent flows. *New J. Phys.* **6**, 35.

Rajagopalan, S. & Antonia, R. A. 1993 Structure of the velocity field associated with the spanwise vorticity in the wall region of a turbulent boundary layer. *Phys. Fluids* A **5** (10), 2502–2510.

Rani, H. P., Sheu, T. W. H. & Tsai, E. S. F. 2007 Eddy structures in a transitional backward-facing step flow. *J. Fluid Mech.* **588**, 43–58.

Rodi, W. 2006 DNS/LES of some engineering flows. *Fluid Dyn. Res.* **38**, 145–173.

Sadeque, M. A. F., Rajaratnam, N. & Loewen, M. R. 2008 Flow around cylinders in open channels. *J. Engng Mech.* **134** (1), 60–71.

Schumann, U. 1975 Subgrid scale model for finite difference simulations of turbulent flows in plane channels and annuli. *J. Comput. Phys.* **18**, 376–404.

Sheu, T. W. H. & Rani, H. P. 2006 Exploration of vortex dynamics for transitional flows in a three-dimensional backward-facing step channel. *J. Fluid Mech.* **550**, 61–83.

Shih, C. & Ho, C.-M. 1994 Three-dimensional recirculating flow in a backward facing step. *J. Fluids Engng* **116**, 228–232.

Simpson, R. L. 1996 Aspects of turbulent boundary-layer separation. *Prog. Aerosp. Sci.* **32**, 457–521.

Snarski, S. R. & Lueptow, R. M. 1995 Wall pressure and coherent structures in a turbulent boundary layer on a cylinder in axial flow. *J. Fluid Mech.* **286**, 137–171.

Song, S. & Eaton, J. K. 2004 Flow structures of a separating, reattaching, and recovering boundary layer for a large range of Reynolds number. *Exp. Fluids* **36**, 642–653.

Spalart, P. R. & Coleman, G. N. 1997 Numerical study of a separation bubble with heat transfer. *Eur. J. Mech.* – B/*Fluids* **16** (2), 169–189.

Spalart, P. R. & Strelets, M. K. 2000 Mechanisms of transition and heat transfer in a separation bubble. *J. Fluid Mech.* **403**, 329–349.

Weber, D. J. & Danberg, J. E. 1992 Correlation of mean velocity measurements downstream of a swept backward-facing step. *AIAA J.* **30**, 2701–2706.

Webster, D. R., DeGraaff, D. B. & Eaton, J. K. 1996 Turbulence characteristics of a boundary layer over a swept bump. *J. Fluid Mech.* **323**, 1–22.

Wilhelm, D., Härtel, C. & Kleiser, L. 2003 Computational analysis of the two-dimensional–three-dimensional transition in forward-facing step flow. *J. Fluid Mech.* **489**, 1–27.

Wood, D. H. & Bradshaw, P. 1982 A turbulent mixing layer constrained by a solid surface. Part 1. Measurements before reaching the surface. *J. Fluid Mech.* **122**, 57–89.

Wu, X. A. & Squires, K. D. 1998 Numerical investigation of the turbulent boundary layer over a bump. *J. Fluid Mech.* **362**, 229–271.

Zang, T. A. 1991 On the rotational and skew-symmetric forms for incompressible flow simulations. *Appl. Numer. Math.* **7**, 27–40.